52nd AIAA/ASME/ASCE/AHS/ASC Structures, Structural Dynamics and Materials Conference
 19th
4 - 7 April 2011, Denver, Colorado

AIAA 2011-1963

Enhanced Modal Solutions for Structural Dynamics in Aerothermoelastic Analysis

Nathan J. Falkiewicz* and Carlos E. S. Cesnik†

Department of Aerospace Engineering, University of Michigan, Ann Arbor, Michigan 48109-2140, USA

Hypersonic vehicle design and simulation require models that are of low order. Modeling of hypersonic vehicles is complicated due to complex interactions between aerodynamic heating, heat transfer, structural dynamics, and aerodynamics in the hypersonic regime. This work focuses on the development of efficient modal solutions for structural dynamics of hypersonic vehicle structures under transient thermal loads. The problem is outlined and aerothermoelastic coupling mechanisms are described. A previously developed reduced-order, time-domain aerothermoelastic simulation framework is used as the starting point for this study. This paper focuses on three main modeling areas: 1) The effect of aerodynamic heating on the evolution of free vibration modes shapes and frequencies is examined, 2) A surrogate modeling technique is employed for directly updating the generalized stiffness matrix and thermal loads based on the transient temperature distribution and 3) Basis augmentation techniques are employed in order to obtain more accurate solutions for the structural dynamic response. The techniques to be studied are described and applied to a representative hypersonic vehicle elevator structure.

Nomenclature

A	= snapshot matrix
$a^{(j)}$	= j-th POD snapshot
b	= vector of inputs to function
$C(b, X)$	= kriging correlation matrix
C	= correlation matrix
c	= vector of POD modal coordinates
$\tilde{c}$	= vector of POD modal coordinates for transformed system
c_p	= specific heat at constant pressure
d	= structural modal coordinates, kriging sample point
E	= modulus of elasticity
F_T	= thermal load vector of full system in physical space
F_S	= structural load vector of full system in physical space
Full	= solution vector of full-order model
f_T	= generalized thermal load vector of reduced system in modal space
f_S	= generalized structural load vector of reduced system in modal space
$G(X^{(i)}, X^{(j)})$	= Gaussian correlation function for kriging model
H_i	= coefficient matrices in numerical integration for structural response
h	= altitude
h_i	= thickness of i-th layer of thermal protection system
K_T	= thermal conductivity matrix of full system in physical space
K_G	= geometric stiffness matrix
K_S	= structural stiffness matrix

*Ph.D. Candidate, Dept. of Aerospace Engineering, University of Michigan, 1320 Beal Ave, Ann Arbor, MI 48109, Student Member AIAA.

†Professor of Aerospace Engineering, Dept. of Aerospace Engineering, University of Michigan, 1320 Beal Ave, Ann Arbor, MI 48109, Associate Fellow AIAA.

K_S^* = modified structural stiffness matrix
k_S^* = generalized stiffness matrix of reduced system in modal space
k_T = generalized thermal conductivity matrix of reduced system in modal space
L = lower triangular factor in decomposition of K_S^*
L_∞ = L_∞ error
l = number of augmented mode shapes
lb_i = lower bound for i-th POD modal coordinate
M = Mach number
M_T = thermal capacitance matrix of full system in physical space
M_S = structural mass matrix of full system in physical space
m_T = generalized thermal capacitance matrix of reduced system in modal space
m_S = generalized mass matrix of reduced system in modal space
$\text{MAC}_{i,j}$ = modal assurance criterion value corresponding to modes i and j
$\max_i$ = maximum value of i-th POD modal coordinate
$\min_i$ = minimum value of i-th POD modal coordinate
MS = margin of safety with respect to POD bounds
NRMSE = normalized root mean squared error
n = number of aerothermoelastic simulations used to generate bounds
n_b = number of basis terms used in kriging regression model
n_{dv} = number of design variables in kriging model
n_e = number of kriging evaluation cases
n_F = number of specified load vectors in load-dependent Ritz vector algorithm
n_k = number of kriging sample points
n_{POD} = number of POD snapshots
n_p = number of output parameters in kriging snapshot
n_R = number of load-dependent Ritz vectors per specified load vector
n_V = number of free vibration modes used in structural basis
$\mathcal{O}$ = order of kriging regression model
p_k = kriging fitting parameter in correlation function
q = number of kriging output quantities
R = kriging regression function
R_x = matrix of kriging basis functions evaluated at each snapshot
ROM = solution vector of reduced-order model
r = number of DOFs of reduced system
r_x = vector of kriging regression functions
s = number of DOFs of full-order system
T = vector of discrete nodal temperatures
$\tilde{T}$ = excess of temperature over initial conditions
$\mathcal{T}_0$ = scalar value of uniform initial temperature distribution
t = time
t_E = time to evaluate kriging model
t_K = time to generate kriging model
t_T = time to generate kriging training data
U = upper triangular matrix, transformation between x_u^R and x_r
ub_i = upper bound for i-th POD modal coordinate
w_a = prescribed z-direction displacements at attachment point
X = matrix of kriging sample points for training data
x = structural degrees of freedom in physical space
$Y(x)$ = snapshot matrix of training data for kriging model
$y_i^{(j)}$ = i-th entry of response vector for j-th kriging snapshot
$\hat{y}(b)$ = kriging approximation to function at point b
$Z(b, X)$ = realization of stochastic process with zero mean and variance σ^2
$z(X)$ = stochastic process vector evaluated at each kriging snapshots

α = angle of attack
α_T = coefficient of thermal expansion

β = coefficients of basis functions in kriging regression model
Δt = time step size
ϵ_i = percentage error at degree of freedom i
η = coefficient in time-dependence of attachment point motion
θ_k = kriging fitting parameters in correlation function
κ = thermal conductivity of material
ν = Poisson's ratio
ρ = density of material
σ = variance
Φ_S = modal matrix of structural reference modes
Φ_T = modal matrix of full set of thermal POD basis vectors
$\bar{\Phi}_T$ = modal matrix of truncated set of POD basis vectors
$\phi^{(j)}$ = j-th free vibration mode
$\varphi^{(j)}$ = j-th thermal basis vector
$\psi^{(i)}$ = i-th load-dependent Ritz vector
$\bar{\psi}^{(i)}$ = i-th load-dependent Ritz vector before normalization
ω = circular frequency in time-dependence of attachment point motion

Subscripts
0 = initial
AE = aeroelastic
AT = aerothermal
HT = heat transfer
I = user-determined input
h = heated
L = lower bound
max = maximum application temperature
r = restrained
U = upper bound
u = unheated, unrestrained

Superscripts
-1 = matrix inverse
A = component of structural load vector due to aerodynamic pressure
a = approximate
BC = reaction force exerted by body on control surface
E = elastic
H = component of structural load vector due to heating
(n) = time level
R = rigid
T = matrix transpose

I. Introduction

Design and simulation of hypersonic vehicles (HSVs) require consideration of a variety of disciplines due to the highly coupled nature of their flight regime.[1] In order to capture all of the potential effects on vehicle dynamics, one must consider the aerodynamics, aerodynamic heating, heat transfer, and elastic airframe as well as the interactions between these disciplines. The problem is further complicated by the large computational expense involved in capturing all of these effects and their interactions in a full-order sense. While high-fidelity modeling techniques exist for each of these disciplines, the use of such techniques is computationally infeasible in a vehicle design and simulation setting for such a highly coupled problem. Early in the design stage, many iterations of analyses may need to be carried out as the vehicle design matures, thus requiring quick analysis turn-around time. Additionally, the number of states and number of degrees of freedom used in the analyses must be small enough to allow for efficient control simulation and design. As a result, alternative approaches must be considered for vehicle simulations.

There are two methodologies that can be utilized in the generation of low-order models. The first

approach is to apply simplifying assumptions that enable the use of first-principles models. These models are characterized by their low-order form and they can often be solved analytically, thus preventing the need to time-march the solution. While these models are useful in generating a low order representation of the physics, the simplifying assumptions made to employ these models often preclude the ability to model detailed geometries or complex physics. This work therefores make use of an alternative approach which involves the use of reduced-order models (ROMs) that are derived from high-fidelity analysis tools. Use of high-fidelity tools alone is infeasible due to their high order and long run time. Thus, this study seeks to go beyond simply coupling existing high-fidelity codes and routines, and instead proposes to use the output of these tools along with model reduction techniques to generate computationally tractable systems of governing equations. The objective of the current work is to make aerthermoelastic simulation of complex geometries feasible without the need for *a priori* assumptions regarding the physics of the problem. As opposed to a first-principles modeling approach, by first modeling as much of the physics as possible and then systematically reducing the order of the system, we can control and quantify the error incurred through model reduction. This also allows for tailoring of the number of states and degrees of freedom as different levels of fidelity may be required as the vehicle configuration matures.

I.A. Previous Work on Aerothermoelastic Modeling

A variety of studies on hypersonic aerothermoelasticity have focused on the aerothermoelastic response and stability of panels with various degrees of aerothermoelastic coupling. A review paper summarized various analytical methods for nonlinear panel flutter at supersonic and hypersonic speeds.[2] The methods are grouped into two main areas: 1) classical methods including Galerkin in conjunction with numerical integration, harmonic balance, and perturbation methods, and 2) finite element methods in the frequency or time domain. Two specific studies[3,4] considered nonlinear panel flutter for high-Mach-number flows under aerothermoelastic effects. These studies both made use of von Kármán plate theory for large displacements and both include geometric nonlinearity due to compressive load. The panel temperature was taken to be equal to the instantaneous flow temperature and was assumed to be uniform to allow for a lumped-capacity approach to the solution of the heat transfer equations. Two related works used an explicit Taylor-Galerkin algorithm to solve the coupled fluid-thermal-structural equations to assess the impact of aerothermoelastic effects on leading edges[5] and panels.[6] These works employed an integrated finite-element approach which solved the Navier-Stokes equations, energy equation, and quasi-static structural equations of motion in an integrated framework. Results from both works showed that structural deformation has a strong effect on flow properties and that severe aerodynamic heating can lead to large stresses due to steep temperature gradients. Another work[7] focused on the thermal analysis of thermal protection panels in hypersonic flow under an imposed deflection. The framework consisted of a finite volume Navier-Stokes CFD code coupled with a boundary element formulation of the transient heat transfer process. The ability of the framework to handle deflection was assessed by imposing a deformed structural configuration, calculating the thermal boundary conditions over the deformed panel, and solving for the transient temperature distribution.

Recent research on aerothermoelastic stability of a hypersonic vehicle control surface used computational fluid dynamics (CFD) to compute the aerodynamic heating along with finite element thermal and structural models to assess its behavior in hypersonic flow.[8] In these studies the aerodynamic heat flux was found by using rigid-body CFD solutions to compute the adiabatic wall temperature and heat transfer coefficient at the surface of the structure. The resulting thermal boundary conditions were applied to a transient thermal finite element analysis and the resulting temperatures were applied to the structural dynamic finite element model. Free vibration frequencies and mode shapes of the heated structure were calculated under both material property degradation with temperature and thermal stresses at each desired point in time. The mode shapes were used in a modal representation of the equations of motion to obtain the aeroelastic response. Third-order piston theory and Euler aerodynamics were used to obtain the generalized loads. The use of CFD for solution of the aeroheating problem provides capability for capturing complex effects such as shock/boundary layer interaction and 3-D flow effects. However, the computational cost associated with CFD is prohibitive in the control design and simulation setting, and the use of an aerothermal ROM is warranted. While Ref. 8 reduced the order of the equations of motion by applying a truncated set of free vibration mode shapes, an eigenvalue solution was still computed at each desired point in time to update the mode shapes. The current work extends that methodology by using a fixed basis throughout the simulation to avoid the need to solve an eigenvalue problem during the course of the simulation while still reducing the order of the equations of motion.

In two recent studies,[9,10] the flow-thermal-structural coupling of two and three dimensional skin panels in hypersonic flow was performed. In Ref. 9, two dimensional panel flutter analysis of a simply supported HSV skin panel was performed using von Kármán plate theory for the structural dynamic response, piston theory for the unsteady aerodynamics, and Eckert's reference enthalpy method for the aerodynamic heating. Specific attention was given to the effects of using 1-way versus 2-way aerothermal-aeroelastic coupling. The most important coupling mechanism on the flutter boundary was found to be the effect of material property degradation due to elevated temperature. In Ref. 10, a similar study was carried out to assess the effect of aerothermoelasticity on a 3-D HSV skin panel. A 3-D finite element model was used to obtain the structural dynamic response as opposed to von Kármán plate theory. Loads on the structure consisted of aerodynamic pressure loads, fluctuating pressure loads due to sound pressure level in the turbulent boundary layer, and thermal loads due to temperature gradients. Results demonstrated that the signficance of fluid-thermal-structural coupling for quasi-static response prediction is a strong function of in-plane boundary conditions.

The thermoelastic portion of the current work is a continuation of previous studies on reduced-order modeling of the heat transfer and structural dynamics problems.[11–14] The earliest of these[11] introduced the reduced-order thermoelastic modeling framework which utilized Proper Orthogonal Decomposition (POD) for reduction of the thermal problem and a modified modal method for reduction of the structural dynamics problem. A subsequent work[12] employed a quasi-steady aerothermoelastic time-marching procedure to assess the effect of thermal loads on the aerodynamic forces over a control surface. A more recent work[13] described an extension of the previous works to unsteady form and specifically addressed the use of POD with time-dependent boundary conditions.

The thermoelastic ROM framework of Ref. 15 was combined with an aerothermal ROM framework into a unified unsteady aerothermoelastic routine in a more recent work.[14] That paper utilized reduced-order structural dynamic, heat transfer, and aerodynamic heating models in a time-marching simulation framework. The structural and thermal modes were used to parameterize the structural dynamic response and wall temperature to allow for discretization of the parameter space and enable creation of the aerothermal kriging surrogate. The error of each ROM was characterized by comparing against the corresponding full-order models. The average normalized root mean squared errors (NRMSE) of thermal ROM were found to be 2.19% and 4.52% for two particular cases. The average L_∞ errors of the thermal ROM were found to be 16.4% and 28.8% for the same two cases. For the structural ROM, the average NRMSE and L_∞ errors were 8.52% and 28.7%, respectively, for one set of flight conditions. The average CPU time for one iteration of the structural dynamic response was found to be 6.23 s for the full-order model and 4.41 s for the ROM. The structural ROM required the most computational time of the various components of the solution. One objective of the current study is to improve the accuracy of the structural ROMs using various techniques. Additionally, significant computational savings can be obtained by improving the computation time associated with the structural ROM. Therefore, in addition to improving the accuracy of the structural ROMs, the current work will also improve the computational efficiency of the framework by implementing the ability to directly update the generalized stiffness and thermal loads as a function of temperature.

I.B. Aerothermoelastic Simulation Framework

The progress described above has led to further investigation into the aerothermoelastic coupling exhibited in hypersonic flight. A flowchart of overall framework applied in this work is shown in Fig. 1. The process begins with the calculation of the heat flux on the outer surface of the structure at the initial time using the Eckert reference temperature method.[16] With the boundary conditions and initial conditions of the thermal problem known, the transient temperature distribution is marched forward in time. Solution of the heat transfer problem is carried out in modal space using modes from POD to avoid the computational cost of running full-order finite element analysis. Bypassing of the full-order thermal solution via the reduced-order solution is indicated by the gray blocks. This work considers two coupling mechanisms between the thermal solution and structural stiffness. The first involves geometric stiffening due to thermal stresses that occur in the structure due to differential thermal expansion resulting from the spatially varying temperature distribution. The second is due to the temperature-dependence of the Young's modulus resulting from the high temperatures experienced in hypersonic flight. In addition to the thermal effects on the stiffness, the change in temperature also results in thermal loads being applied to the structure. With the stiffness and structural loads known, the structural dynamics system of equations in physical space is transformed to a suitable reduced modal basis to be described in a subsequent section. The reduced modal system is then

solved for the modal coordinates to obtain the structural response. The structural deformations couple with the aerothermal problem due to the effect on aerodynamic flow properties, which change the heat flux. The deformations also result in a change in aerodynamic pressures which modify the structural loads. With the deformed configuration known at the current time step, the unsteady aerodynamic flow properties are updated using third-order piston theory and the process is repeated at the next time step. Note that the details of the piston theory implementation are given in a previous work.[17] After a pre-determined number of aeroelastic iterations have been carried out, the heat flux boundary conditions are recalculated and the thermal solution is updated.

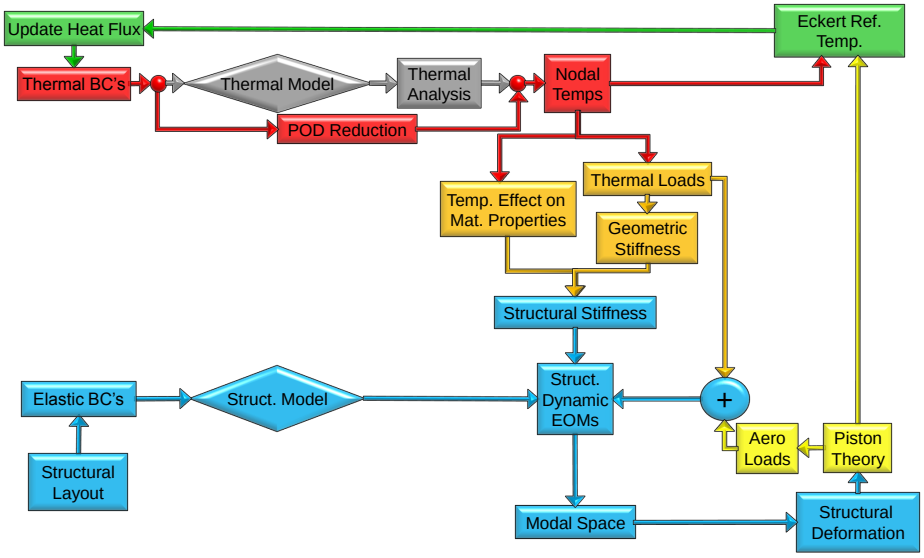

Figure 1. Reduced-order aerothermoelastic modeling framework.

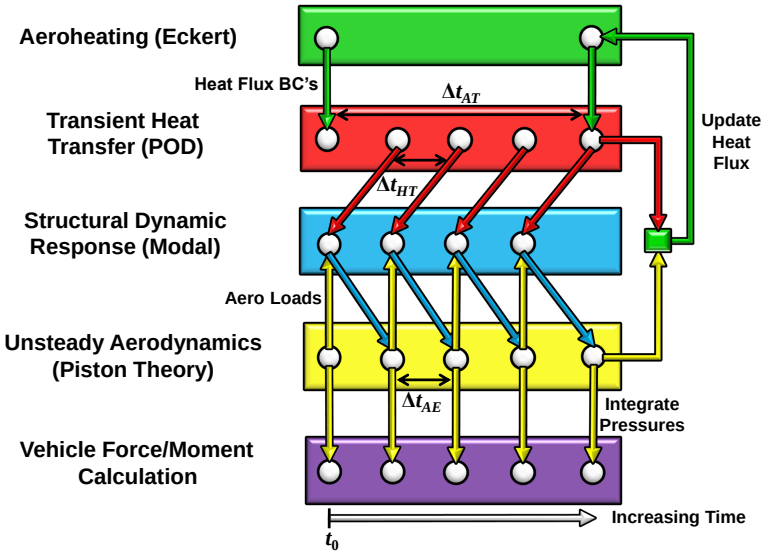

Figure 2. Overview of aerothermoelastic time-stepping schedule.

A time-marching procedure with updates to the thermal and structural boundary conditions at specified intervals is proposed for solution of the coupled aerothermoelastic problem. An outline of the time-stepping schedule is given in Fig. 2. The size of the aeroelastic time step, Δt_{AE}, is smaller than the size of the aerothermal time step, Δt_{AT}, due to the fact that the aeroelastic time scale is faster than the thermal time scale. The procedure begins by calculating the aerodynamic flow properties over the undeformed structure at initial time, t_0. Using the flow properties, the heat flux at the outer surface is found along with the local skin

friction coefficients using the Eckert reference temperature method. The aerodynamic pressures and viscous drag components are then integrated to determine the aerodynamic forces and moments at initial time. With the thermal boundary conditions known, a pre-determined number of thermal time steps are taken, each of size Δt_{HT}, until the time $t_0 + \Delta t_{AT}$ is reached. The thermal loads based on the temperature change between t_0 and $t_0 + \Delta t_{AE}$ are then applied to the structural configuration at t_0. Additionally, the aerodynamic loads based on the already calculated flow properties are applied to the structure. The structural dynamic response solution is then marched forward one time step of size Δt_{AE}. The displacements are fed back into the aerodynamic solver and the flow properties are calculated at time $t_0 + \Delta t_{AE}$ over the updated deformed configuration. Each time the flow properties are re-calculated, the aerodynamic pressures are also integrated to allow for characterization of the transient aerodynamic forces and moments on the vehicle. The aeroelastic iterations continue to be carried for a pre-determined number of time steps. Once the time instant $t_0 + \Delta t_{AT}$ has been reached, the instantaneous flow properties and wall temperatures are used to update the heat flux boundary conditions to the thermal problem. With the updated thermal boundary conditions known, the transient thermal solution is marched forward from the time instant $t_0 + \Delta t_{AT}$ to the time instant $t_0 + 2\Delta t_{AT}$ and the process is repeated.

II. Proper Orthogonal Decomposition for Reduced-Order Thermal Solution

This work makes use of POD for reduced-order solution of the transient thermal problem. POD, also known as the Karhunen-Loève decomposition, principal components analysis, singular systems analysis, and singular value decomposition, is a modal technique in which empirical data is processed using statistical methods to obtain models which capture the dominant physics of a system using a finite number of modes.[18] The fundamental basis for use of POD as a reduced-order modeling method is its ability to represent high-dimensional systems in a low-dimensional, approximate manner while still maintaining a high degree of accuracy. The choice of the POD basis as opposed to any other basis such as an eigenvector basis is due to its optimality condition of providing the most efficient way of capturing the dominant components of a system with a finite number of modes.[19]

The method of snapshots[20] is used for determination of the POD basis vectors. In this case, the snapshots are defined as vectors of nodal temperatures at various time instants and are computed from high-fidelity finite element analysis. The goal of the POD formulation is to express the vector of nodal temperatures, T, at any time instant as a linear combination of the basis, $\varphi(x, y, z)$, with coefficients $c(t)$, i.e.,

$$\begin{Bmatrix} T_1(t) \\ \vdots \\ T_s(t) \end{Bmatrix} = c_1(t) \begin{Bmatrix} \varphi_1^{(1)} \\ \vdots \\ \varphi_s^{(1)} \end{Bmatrix} + c_2(t) \begin{Bmatrix} \varphi_1^{(2)} \\ \vdots \\ \varphi_s^{(2)} \end{Bmatrix} + \cdots + c_r(t) \begin{Bmatrix} \varphi_1^{(r)} \\ \vdots \\ \varphi_s^{(r)} \end{Bmatrix}, \tag{1}$$

where s is the total number of degrees of freedom in the finite element model and r is the total number of POD basis vectors retained after truncation. The basis is computed by first generating the snapshot matrix, A, given by,

$$A = \begin{bmatrix} T_1^{(1)} & T_1^{(2)} & \dots & T_1^{(n_{POD})} \\ T_2^{(1)} & T_2^{(2)} & \dots & T_2^{(n_{POD})} \\ \vdots & \vdots & \ddots & \vdots \\ T_s^{(1)} & T_s^{(2)} & \dots & T_s^{(n_{POD})} \end{bmatrix} = \left[a^{(1)}, a^{(2)}, \dots, a^{(n_{POD})} \right], \tag{2}$$

where $T_i^{(j)}$ indicates the i-th entry of the j-th snapshot, n_{POD} is the number of snapshots taken, and $a^{(j)}$ refers to the column vector corresponding to the j-th snapshot. An eigendecomposition or singular value decomposition is used to obtain the POD modal matrix, Φ_T. Based on the eigenvalues corresponding to each of the POD modes, the dominant POD modes are identified and the truncated POD modal matrix, $\bar{\Phi}_T$, is formed. Detailed explanation of POD basis creation is given in a previous work by the authors,[13] and is thus omitted here for brevity.

The advantage to using POD is that the computationally-intensive process of generating the basis is carried out *a priori*, and the basis is not updated throughout the simulation. Once the basis has been created, it is applied to the full-order system of heat transfer equations in order to reduce its size. Consider

the full-order system of first order coupled ordinary differential equations governing transient heat transfer,

$$M_T\dot{T}(t) + K_T T(t) = F_T(t), \tag{3}$$

where M_T is the thermal capacitance matrix, K_T is the thermal conductivity matrix, and F_T is the thermal load vector. The first step of the reduction process is to project the full-order system onto the truncated POD basis and transform from physical space to modal space using

$$\bar{\Phi}_T^T M_T \bar{\Phi}_T \dot{c}(t) + \bar{\Phi}_T^T K_T \bar{\Phi}_T c(t) = \bar{\Phi}_T^T F_T(t). \tag{4}$$

The generalized thermal capacitance matrix, m_T, generalized thermal conductivity matrix, k_T, and generalized load vector, f_T, are then identified such that

$$m_T = \bar{\Phi}_T^T M_T \bar{\Phi}_T \tag{5a}$$

$$k_T = \bar{\Phi}_T^T K_T \bar{\Phi}_T \tag{5b}$$

$$f_T(t) = \bar{\Phi}_T^T F_T(t). \tag{5c}$$

Note that because the POD basis vectors are not eigenvectors of the generalized eigenvalue problem, m_T and k_T are not diagonal at this stage. As the time-dependence of the thermal load vector is not known ahead of time, there is little advantage to diagonalizing the system and solving each equation analytically. Thus, the coupled system is integrated numerically in modal space using a second-order Crank-Nicolson scheme as described in a previous work by the authors.[13]

III. Reduced-Order Modal Basis Solution for Structural Dynamic Response

While the full-order system of structural dynamic equations of motion is used for comparison purposes, its solution within the aerothermoelastic framework presented here is not suitable for vehicle design and control analysis purposes. The problem of solving for the structural dynamic response of hypersonic vehicle structures within a design and simulation framework is complicated by various factors. Due to the large number of degrees of freedom involved in a traditional finite element solution, steps must be taken to reduce the order of the structural dynamics system of equations. A common approach is to employ a modal transformation in which the structural displacements are expressed as a linear combination of a small number of basis vectors which are the free vibration mode shapes of the structure. However, this approach cannot be applied directly for hypersonic vehicle applications as the mode shapes change over time due to modification of the stiffness from geometric stiffness and material degradation effects. The approach taken in this work is to first perform an off-line calculation and select a reduced number of Ritz modes based on the free vibration modes of the structure at a reference temperature distribution. These Ritz modes are then used as the modal basis for solution of the structural response throughout the simulation. This procedure is applicable as the Ritz modes need only to satisfy the geometric boundary conditions,[21] which will always be the case regardless of the stiffness distribution. The modal matrix containing the structural reference modes, Φ_S, is not updated throughout the simulation, thus preventing the need to solve an eigenvalue problem of the full system during the course of the simulation. Though the reference modes are not updated throughout the simulation, the stiffness matrix is updated each time the structural dynamic response is calculated to account for its dependence on temperature. Updating of the conventional stiffness matrix is performed using the temperature-dependence of the material properties of the various materials. The geometric stiffness matrix is updated by solving a static finite element problem based on the thermal loads from temperatures at the current time step and the material coefficients of thermal expansion to calculate the internal loads.

The full-order system of structural dynamic equations of motion in physical space is given by

$$M_S\ddot{x}(t) + K_S^*(T)x(t) = F_S^H(t) + F_S^A(t), \tag{6}$$

where M_S is the mass matrix, F_S^H is the load vector due to heating, F_S^A is the load vector due to aerodynamic pressure, and x are the physical degrees of freedom. Note that F_S^A contains a normal pressure component calculated using the third-order piston formulation as well as a wall shear stress component calculated using the local element skin friction coefficients obtained from the Eckert reference temperature computation. A description of the formulation used to compute the local skin friction coefficients is given in a previous work by the authors.[15] The modified stiffness matrix, K_S^*, is given by

$$K_S^*(T) \equiv K_S(T) + K_G(T), \tag{7}$$

where $K_S(T)$ is the conventional stiffness matrix that varies due to the temperature-dependence of the material properties and $K_G(T)$ is the geometric stiffness matrix resulting from thermal stresses. The reduced-order system is obtained by first expressing an approximation to the physical degrees of freedom, $x^a(t)$, as a linear combination of the structural basis vectors such that

$$x^a(t) = \Phi_S d(t), \tag{8}$$

where d represents the modal coordinates of the reference modes which are stored as columns of the modal matrix, Φ_S. Note that since the number of reference modes used in the modal expansion is much less than the number of physical degrees of freedom in the model, the computational cost of the numerical solution of the system is relatively inexpensive. Once the modified stiffness matrix is known at the current time instant, the system is reduced by substituting Eq. (8) into Eq. (6) and pre-multiplying the system by Φ_S^T, i.e.

$$\Phi_S^T M_S \Phi_S \ddot{d}(t) + \Phi_S^T K_S^*(T) \Phi_S d(t) = \Phi_S^T \left[F_S^H(t) + F_S^A(t) \right]. \tag{9}$$

The generalized mass matrix, m_S, generalized stiffness matrix, k_S^*, generalized load vector due to heating, f_S^H, and generalized load vector due to aerodynamic pressure, f_S^A, are then given by

$$m_S = \Phi_S^T M_S \Phi_S \tag{10a}$$
$$k_S^*(T) = \Phi_S^T K_S^*(T) \Phi_S \tag{10b}$$
$$f_S^H(t) = \Phi_S^T F_S^H(t) \tag{10c}$$
$$f_S^A(t) = \Phi_S^T F_S^A(t). \tag{10d}$$

As the mass of the structure is taken to be constant in this work, the reference modes are orthogonal with respect to the mass matrix and the generalized mass matrix, m_S, reduces to the identity matrix.

Since the modified stiffness matrix is continuously changing, we have no guarantee of orthogonality of the reference modes with respect to stiffness, and the equations are coupled. As such, the reduced-order system of equations in modal space is integrated numerically to calculate the vector of modal coordinates at each time instant. As the high-fidelity structural dynamic response solution is treated as the truth model, the numerical integration scheme used for the high-fidelity model (based on Nastran Sol 109) is implemented for solution of the reduced-order system for the modal coordinates, $d(t)$, to eliminate any discrepancies in the response due to differences in numerical integration schemes. The numerical integration method is similar to the Newmark-β method except that the load vector is averaged over three time instants and the stiffness matrix is modified such that the dynamic equation of motion reduces to a static solution if no inertial effects or damping exists.[22] The scheme uses a central finite difference representation for the velocity and acceleration at discrete times, given by[22]

$$\dot{d}^{(n)} = \frac{1}{2\Delta t_{AE}} \left(d^{(n+1)} - d^{(n-1)} \right) \tag{11a}$$
$$\ddot{d}^{(n)} = \frac{1}{\Delta t_{AE}^2} \left(d^{(n+1)} - 2d^{(n)} + d^{(n-1)} \right), \tag{11b}$$

where the superscript (n) refers to the time level. The initial conditions, $d^{(0)}$ and $\dot{d}^{(0)}$, are used to generate the vectors $d^{(n-1)}$, $f_S^{(n-1)}$, and $f_S^{(n)}$ for the initial time step, $n = 0$, using

$$\dot{d}^{(-1)} = d^{(0)} - \dot{d}^{(0)} \Delta t_{AE} \tag{12a}$$
$$f_S^{(-1)} = k_S^* d^{(-1)} \tag{12b}$$
$$f_S^{(0)} = k_S^* d^{(0)}. \tag{12c}$$

Note that this formulation assumes that the inital acceleration for all points is zero (initial velocity is constant). Substituting the finite difference approximations of the velocity and accelerations, Eqs. (11), into the equations of motion, Eq. (6), and averaging the applied loads over three adjacent time instants, the equations of motion are re-written as

$$H_1 d^{(n+1)} = H_2 + H_3 d^{(n)} + H_4 d^{(n-1)}, \tag{13}$$

where,

$$H_1 = \frac{1}{\Delta t_{AE}^2} m_S + \frac{1}{3} k_S^* \tag{14a}$$

$$H_2 = \frac{1}{3}\left(f_S^{(n+1)} + f_S^{(n)} + f_S^{(n-1)}\right) \tag{14b}$$

$$H_3 = \frac{2}{\Delta t_{AE}^2} m_S - \frac{1}{3} k_S^* \tag{14c}$$

$$H_4 = \frac{-1}{\Delta t_{AE}^2} m_S - \frac{1}{3} k_S^*. \tag{14d}$$

The solution vector at the next time step, $d^{(n+1)}$, is obtained by decomposing H_1 and applying it to the right-hand side of Eq. (13).

IV. Overview of ROM Generation Process

As some of the ROMs used in the aerothermoelastic simulation process are dependent on components of other ROMs, these models must be generated in a specific order. An overview of the process is given in Fig. 3. The green blocks in the figure describe the process for generating a kriging-based aerothermal ROM developed by Crowell et al.[23] and incorporated into the ROM framework in a recent work.[14] Because the current work is focused on structural dynamic and thermal ROM components, the Eckert reference temperature method is utilized in place of the aerothermal ROM here. However, the aerothermal ROM component is included in Fig. 3 to illustrate the complete ROM generation process. The first ROM to be created is the POD model for the transient thermal component of the solution. To begin, the range of vehicle flight parameters is defined. Based on these parameters, represenative simulations are defined for use in extracting the POD snapshots. Because the aerothermal ROM is dependent on the thermal ROM, the Eckert reference temperature method is used to calculate the heat flux in these simulations. Additionally, the structural dynamic ROM is dependent on the thermal ROM, and thus the high-fidelity structural model is used in these simulations. The accuracy of the thermal ROM is evaluated by running representative aerothermoelastic simulations using both the thermal ROM and full-order model and comparing their output. If greater accuracy is desired, more snapshots are taken and the thermal ROM is updated.

Once an accurate thermal ROM has been created, the next step is to identify the reference thermal state at which to evaluate the structural reference modes. The philosophy used in this work is to take the reference thermal state to be the average nodal temperatures over the thermal snapshots. Based on the frequency range of interest, a set of free vibration modes are evaluated at the reference thermal state including both material property degradation with temperature and geometric stiffening due to thermal stresses. Additionally, static modes are extracted based on representative loading conditions. In order to evaluate the accuracy associated with the modal basis, kriging ROMs of the stiffness matrix and thermal load vector (described in section VII) are needed. To generate these ROMs, bounds on the POD modal coordinates are established and kriging training cases are run. At this point, the accuracy of the structural ROM is assessed by again running representative aerothermoelastic simulations and comparing the output of the structural ROM with that of the full-order structural model. If greater accuracy is desired, the structural modal basis is updated and the process is repeated.

The thermal and structural ROMs are then used in the aerothermal ROM generation process developed by Crowell et al.[23] An added benefit to expressing the temperature distribution and deformation as a linear combination of modes is that it allows for parameterization of each in terms of a small number of design variables for the purpose of creating the aerothermal ROM. Bounds on the aerothermal ROM parameters are first established. Parameters for the aerothermal ROM consist of the structural and thermal modal coordinates as well as flight parameters such as angle of attack, Mach number, and altitude. Because the feasible number of parameters in the aerothermal ROM is limited, a subset of thermal and structural modes are used in its creation. Training cases are set up within the parameter space using Latin Hypercube Sampling (LHS). For each training case, CFD analysis is used to generate training data of the aerodynamic heating. Using this training data, a kriging ROM representing the aerodynamic heat flux at the outer surface is generated. The accuracy is then evaluated using a separate set of evaluation cases. If greater accuracy is desired, more kriging sample points are added and the process is repeated. Once a satisfactory aerothermal ROM has been obtained, the ROM generation process is complete and the thermal, structural,

and aerothermal ROMs can then be used for efficient aerothermoelastic simulation.

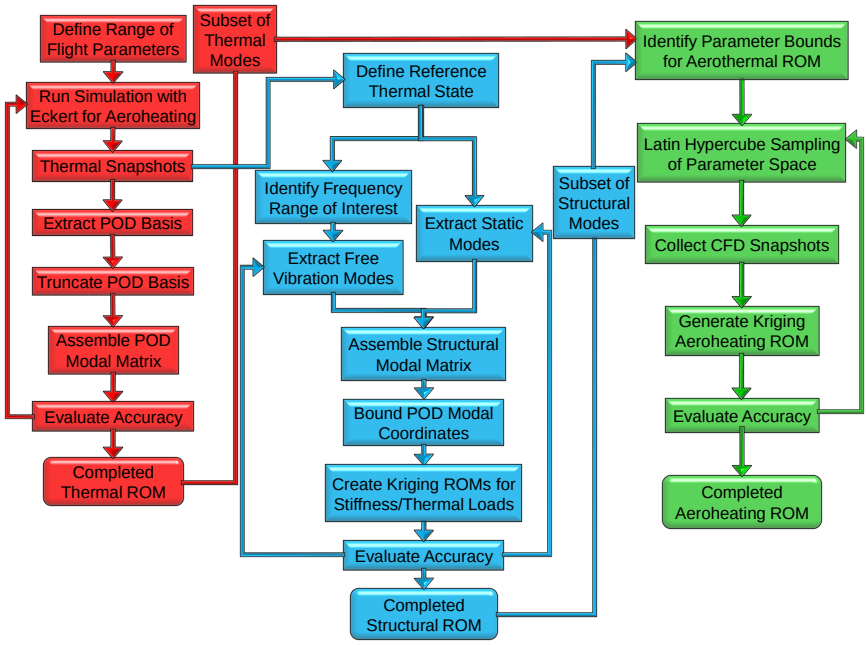

Figure 3. Flowchart of aerothermoelastic ROM generation process.

V. Control Surface Model

The hypersonic vehicle configuration considered in this study, as developed in a previous work,[24] is shown in Fig. 4. A finite element model of a representative hypersonic vehicle elevator has been created for use in this study. The thickness from the top skin layer to the bottom skin layer is 4% chord length.[25] The top and bottom skin layers are each equipped with two 3.8 mm thick thermal protection system layers, and thus the thickness of the outer mold line is 4% chord length plus the 15.2 mm of thermal protection system material. The chord length at the root is 5.2 m. (17 ft.)[24] and the leading edge makes an angle of 34° with the y axis while the trailing edge makes an angle of 18° with the y axis.[26] Planform and cross-sectional views of the airfoil are given in Fig. 5 and Fig. 6, respectively. A survey of the literature revealed a wide range

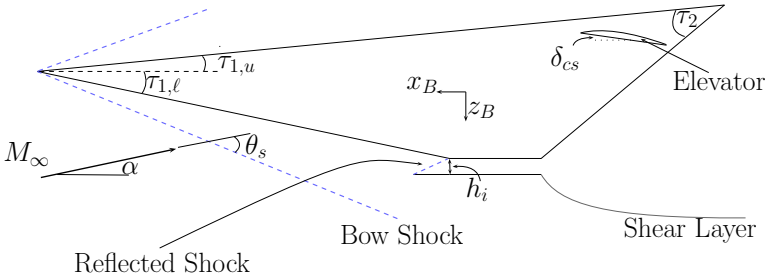

Figure 4. Overall HSV geometry illustrating position of control surface.

of design strategies for mitigating the high temperatures experienced in hypersonic flight.[27–30] This study considers a thermal protection system consisting of an outer heat shield and middle insulation layer on top of the skin as shown in Fig. 7. The material for the heat shield is chosen to be René 41 as it was found to be efficient in terms of mechanical properties at elevated temperatures. For the insulation layer, three different materials were considered in the preliminary materials evaluation: Internal Multiscreen Insulation (IMI), High Temperature Flexible Min-K, and Q-Fiber Felt. Of these, the Min-K insulation, which is a proprietary silica based material faced with Astroquartz cloth,[31] is selected due to its relatively low thermal diffusivity. For the structure (both skin and stiffeners), the Titanium alloy TIMETAL 834 (formerly known

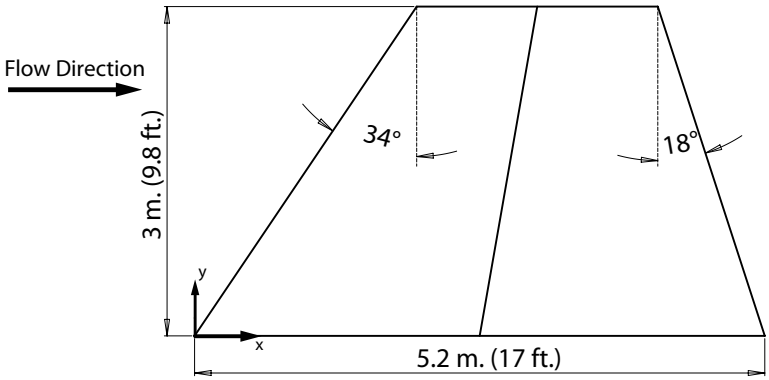

Figure 5. Planform geometry of control surface model.

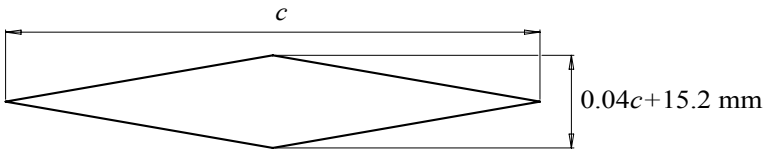

Figure 6. Cross-sectional geometry of control surface model.

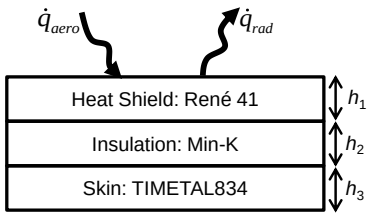

Figure 7. Schematic of material stacking scheme at outer mold line of structure.

as IMI 834) is chosen. The advantage of using this alloy is that its maximum application temperature is 600°C compared with that of Ti-6242S (520°C), Ti-6242 (450°C), Ti-811 (400°C), and Ti-6-4 (300°C).[32] The thermal and mechanical properties of the three materials employed in the model are shown in Table 1, where "T-dep." indicates that the property is temperature-dependent.[26,31,33,34] Note that the temperature-dependent material properties for René 41 are extrapolated beyond the available data and the maximum application temperature, T_{max}, is set to 1500 K. The emissivity of the heat shield is taken to be 0.85.[26] The thermal strain is calculated based on the temperature change with respect to a reference stress-free temperature. The reference temperature used for calculation of thermal strain is taken to be 293 K for all materials.

Table 1. Structural and thermal material properties used in the study.

	ρ $[kg/m^3]$	E $[Pa]$	ν	α_T $[\mu m/m/K]$	κ $[W/m/K]$	c_p $[J/kg/K]$	T_{max} K	h $[mm]$
Heat Shield	8240	T-dep.	0.31	T-dep.	18	541	1500	3.8
Insulation	256	Neglect	Neglect	Neglect	0.052	858	1250	3.8
Skin[a]	4550	T-dep.	0.31	11	7	525	873	6.35

[a] The properties ν, κ, and c_p for TIMETAL 834 were obtained from `http://www.matweb.com/search/DataSheet.aspx?MatGUID=a74096c99aa6486382a9c9e1be0883c4`.

The finite element model used for the thermal and structural modeling aspects of the study is shown in Fig. 8 with the top surface removed for visualization purposes. The model consists of the thermal protection layers system described above along with chordwise and spanwise stiffeners. The material used for the stiffeners is TIMETAL 834 and the thickness of all stiffeners is 25.4 mm (1 in). The model contains 2,812 thermal degrees of freedom and 8,074 structural degrees of freedom. The heat shield and insulation layer are each modeled using 6-node solid wedge elements while the top and bottom skins and stiffeners are modeled using 3-node, 2-dimensional triangular elements. Of the 6,886 elements in the model, 3,456 are solid elements and 3,430 are triangular elements. The control surface is taken to be all-moveable about a hinge line located at the mid-chord[24] and will thus be connected to the vehicle main body through a torque tube. This attachment is modeled by constraining the region indicated by the gray circle in Fig. 8 in all degrees of freedom. In addition, the nodes at the root are constrained against translation in the y direction. Because the stiffness of the insulation layer is neglected, rigid (RBE2) elements are used between each skin node and the corresponding node at the outer surface of the insulation layer to prevent singularities in the solution.

VI. Effect of Transient Heating on Free Vibration Mode Shapes

As described in section III, the structural reference modes are not updated during the course of the aerothermoelastic simulation and it is thus important to characterize the effect of transient heating on the free vibration mode shapes of the structure. To assess this effect, the structural mode shapes under transient heating are computed as a function of time for representative flight conditions. Solution of the free vibration problem includes both material degradation and geometric stiffening effects. The flight conditions for this simulation are taken to be Mach 8 at an altitude of 26 km with an angle of attack of 3° and a uniform initial temperature distribution of 293 K. The heat transfer time step, Δt_{HT}, is taken to be 1 s and the aerothermal time step, Δt_{AT}, is taken to be 5 s. The structure is taken to be rigid for the purposes of unsteady aerodynamics and thus the initial flow properties calculated over the undeformed configuration are held constant for the duration of the simulation. A time history of 2 hours (7,200 s) is obtained from the simulation. Note that the full-order thermal model is used for this simulation to eliminate any errors due to model reduction. Plots of the maximum and minimum nodal temperatures are given in Figs. 9(a) and 9(b), respectively. The maximum temperature approaches an equilibrium value within the duration of the simulation while the minimum temperature is still increasing.

In order to quantitatively assess the evolution in mode shapes due to heating, the modal assurance criterion[35] (MAC) is employed. The MAC is a relation used to estimate the degree of correlation between two mode shape vectors. In this work, the MAC is used to quantify the correlation between the i-th heated

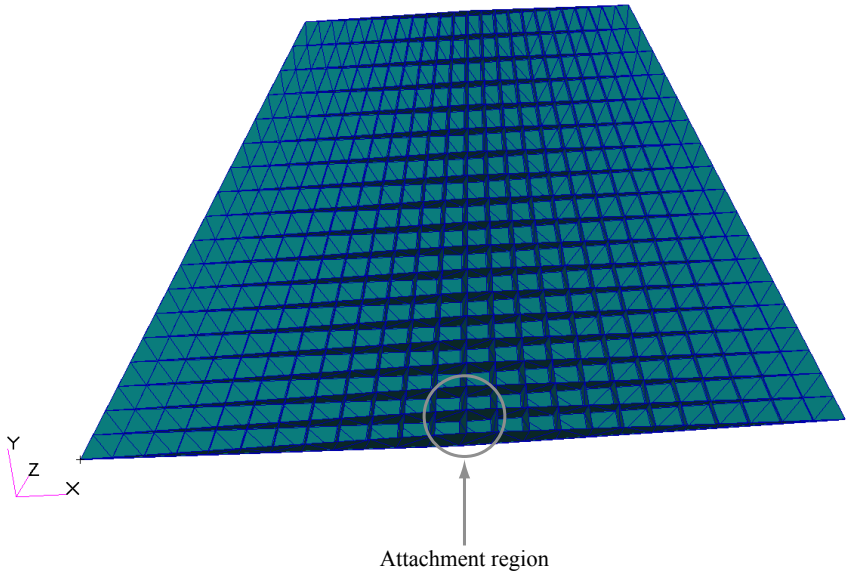

Figure 8. Finite element model of control surface used in study.

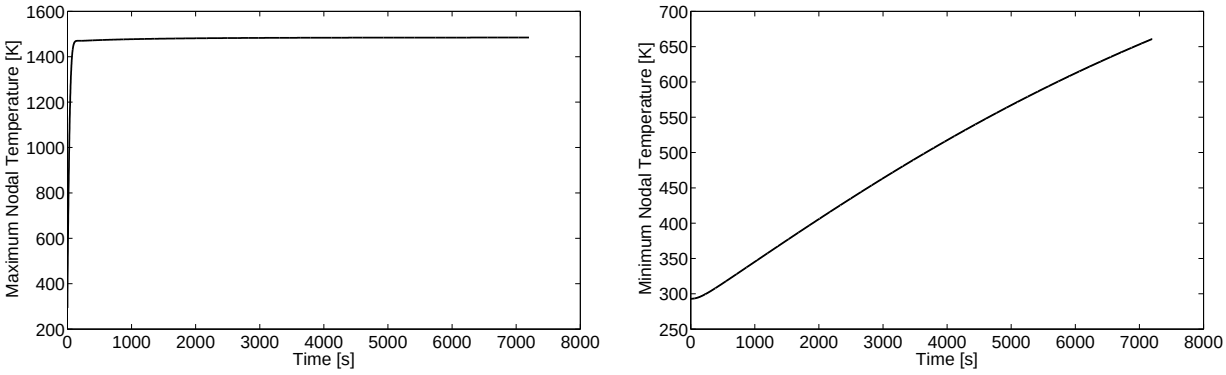

(a) Maximum nodal temperatures.

(b) Minimum nodal temperatures.

Figure 9. Maximum and minimum nodal temperatures vs. time for $M = 8$, $\alpha = 3^\circ$, $h = 26$ km, $T_0 = 293$ K uniform.

mode, $\phi_h^{(i)}$, and the j-th unheated mode, $\phi_u^{(j)}$ at each aeroelastic time step. The unheated modes are taken to be those at the initial uniform temperature distribution of 293 K. The MAC value, $\text{MAC}_{i,j}$, corresponding to the correlation between $\phi_h^{(i)}$ and $\phi_u^{(j)}$ is given by

$$\text{MAC}_{i,j} = \frac{\left|\left(\phi_h^{(i)}\right)^T \left(\phi_u^{(j)}\right)\right|^2}{\left[\left(\phi_h^{(i)}\right)^T \left(\phi_h^{(i)}\right)\right]\left[\left(\phi_u^{(j)}\right)^T \left(\phi_u^{(j)}\right)\right]}. \tag{15}$$

The MAC takes on values between zero and one, where a value of one indicates exact correspondence between modes. A matrix can be assembled by calculating the MAC value relating each heated mode to each unheated mode. The MAC analysis described here considers the first six modes of the structure, and thus the MAC matrix is a 6×6 matrix. The first six unheated mode shapes and frequencies are given in Fig. 10. The first step is to compute the diagonal values of the MAC matrix as a function of time to assess the correspondence between each heated mode and the corresponding unheated mode. This calculation is performed at each heat transfer time step of the simulation. Note that the heated modes are always sorted in order of increasing natural frequency. Plots of the diagonal values of the MAC matrix are given in Fig. 11. As evidenced by the figures, heated modes one, two, five, and six do not deviate significantly from the corresponding unheated modes and the diagonal values of the MAC corresponding to these modes remain close to one. However, for modes three and four there exists a decrease in the MAC value over time, indicating a loss of correspondence with the corresponding unheated modes.

To further explore the evolution of modes three and four over time, off-diagonal terms of the MAC matrix are examined. Specifically, Fig. 12(a) shows $\text{MAC}_{3,3}$ and $\text{MAC}_{3,4}$ over time in order to compare the correspondence between heated mode three and unheated mode three against heated mode three and unheated mode four. Similarly, Fig. 12(b) shows $\text{MAC}_{4,4}$ and $\text{MAC}_{4,3}$ over time. The figures illustrate the fact that heated mode three begins to resemble unheated mode four over time, and heated mode four begins to resemble unheated mode three over time. To visualize how the third heated mode evolves over time, it is plotted at 290 s (the approximate crossover time in Fig. 12(a)) and at 7,200 s (the end of the transient) as shown in Fig. 13. Similarly, the fourth mode is plotted at 440 s (the approximate crossover time in Fig. 12(b)) and at 7,200 s as shown in Fig. 14. Comparing Fig. 13(b) to Fig. 10(d), it is observed that heated mode three is qualitatively similar to unheated mode four at the end of the transient. Similarly, comparing Fig. 14(b) to Fig. 10(c), heated mode four appears qualitatively similar to unheated mode three at the end of the transient.

Plots of the percentage change in the natural frequency of each heated mode with respect to the unheated frequencies are given in Fig. 15. Note that the heated frequencies are sorted in order of increasing increasing magnitude at each time step. For modes $1-3$, the greatest deviation from the unheated frequency is found to be a 7% decrease, while that for modes $4-6$ is found to be a 12% decrease. Thus, in situations where the natural frequency has a significant impact on the system, such as in HSV control system design, the effect of aeroheating on the natural frequencies is important to consider.

These results provide support for the use a fixed basis in the structural dynamic ROM over the duration of the aerothermoelastic simulation. For modes one, two, five, and six, we observe that the corresponding diagonal MAC value remains close to one, and thus there is not a significant loss in accuracy by not updating the basis as the structure is heated. Though mode switching occurs between heated modes three and four, at any time during the evolution of the mode shapes each contain contributions primarily from unheated modes three and four. Thus, either of these heated modes can also be well represented at any instant in time using the unheated modes, and no update of the modes is necessary as the structure is heated.

VII. Efficient Updating of Stiffness and Thermal Loads

VII.A. Overview of Kriging Theory

As the temperature distribution of the structure is continuously changing in time, the stiffness matrix and thermal load vector must be updated at every iteration of the structural dynamic response solution. Calculation of the generalized stiffness involves generating the physical stiffness matrix and pre- and post-multiplying by the modal matrix. Updating the physical stiffness matrix requires assembling $K_S(T)$ based on the temperature-dependence of material properties as well as solving a linear static finite element problem to

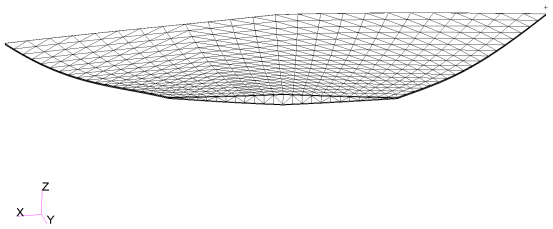

(a) Mode 1: 25.5 Hz.

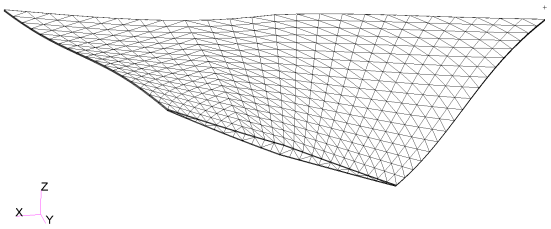

(b) Mode 2: 37.2 Hz.

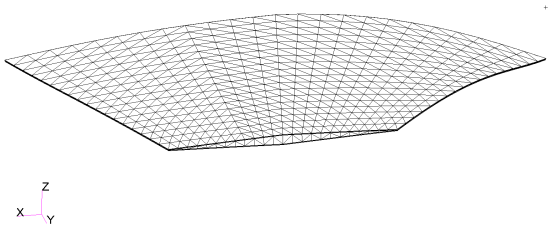

(c) Mode 3: 54.5 Hz.

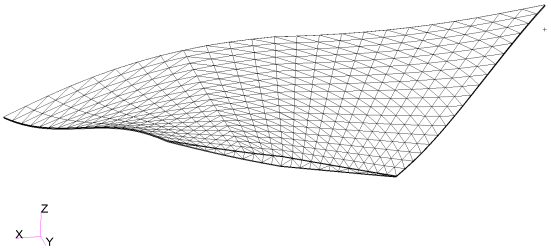

(d) Mode 4: 56.6 Hz.

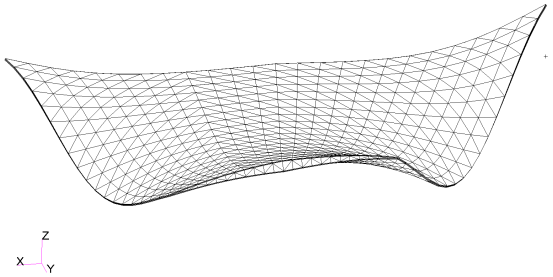

(e) Mode 5: 92.2 Hz.

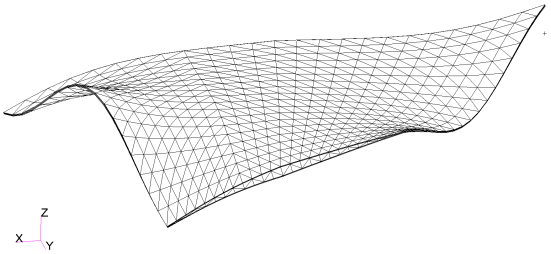

(f) Mode 6: 104.4 Hz.

Figure 10. First six unheated mode shapes and frequencies.

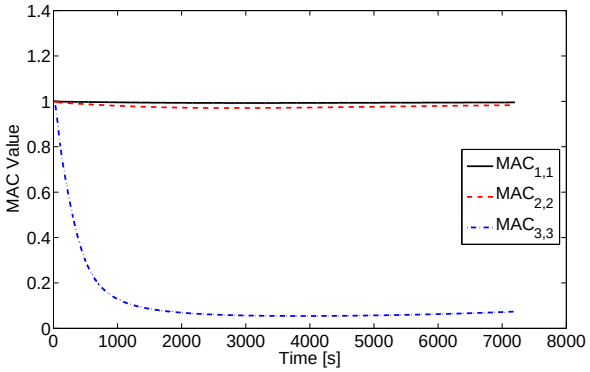

(a) Modes 1–3.

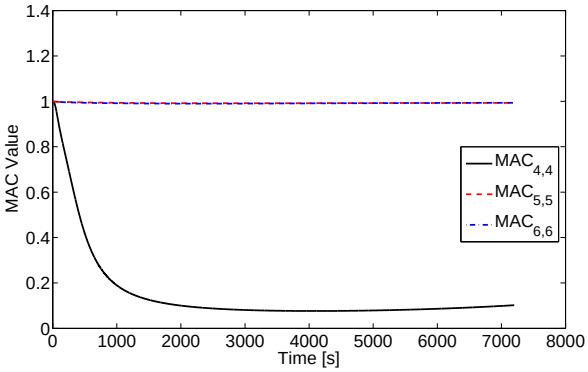

(b) Modes 4–6.

Figure 11. Diagonal entries of MAC matrix for first six modes vs. time.

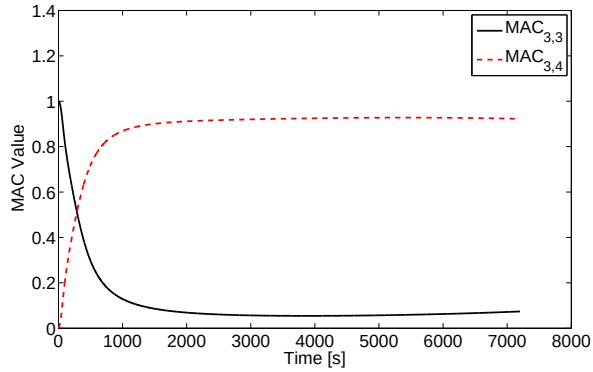

(a) $MAC_{3,3}$ vs. $MAC_{3,4}$.

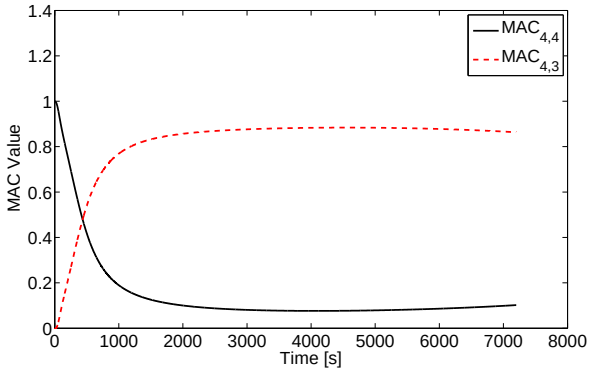

(b) $MAC_{4,4}$ vs. $MAC_{4,3}$.

Figure 12. Comparison of diagonal and off-diagonal entries of MAC matrix for third and fourth modes vs. time.

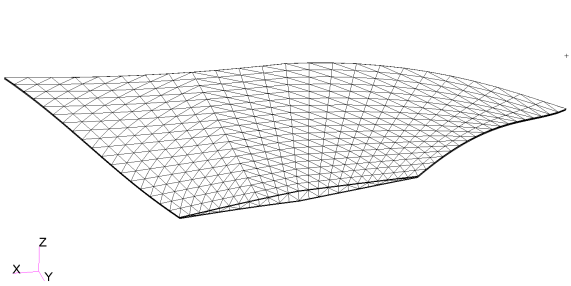

(a) Mode 3 at 290 s: 53.7 Hz.

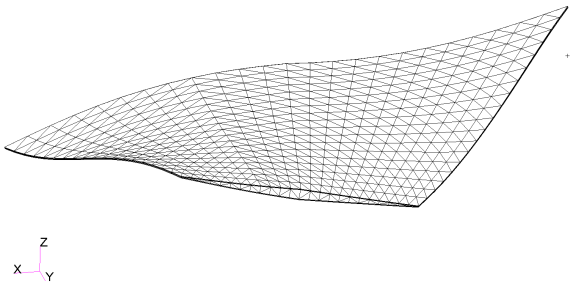

(b) Mode 3 at 7,200 s: 53.1 Hz.

Figure 13. Mode 3 at two different time instants showing evolution of mode shape with heating.

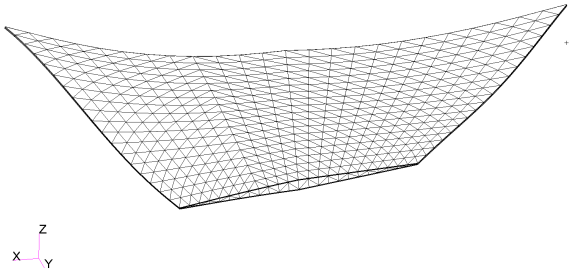

(a) Mode 4 at 440 s: 54.2 Hz.

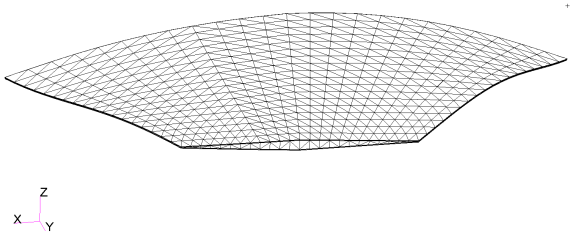

(b) Mode 4 at 7,200 s: 54.1 Hz.

Figure 14. Mode 4 at two different time instants showing evolution of mode shape with heating.

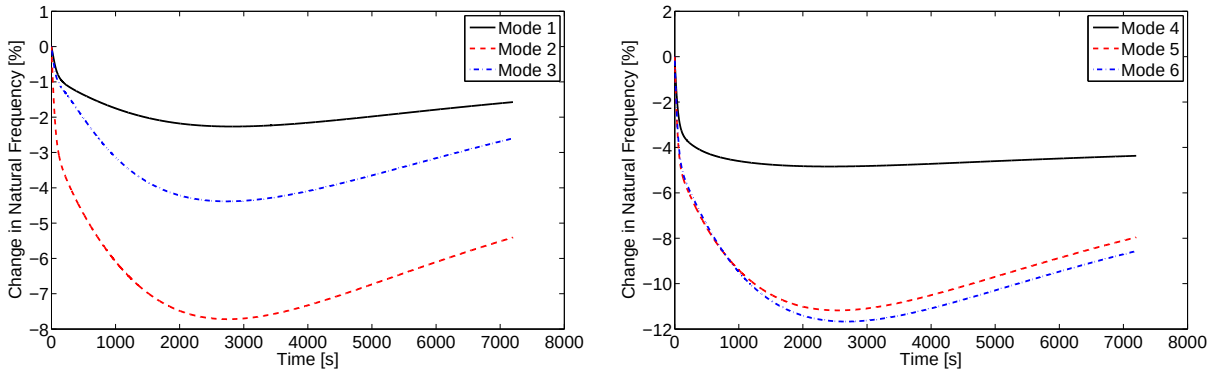

(a) Heated modes 1–3.

(b) Heated modes 4–6.

Figure 15. Percentage change in natural frequencies of first six heated modes vs. time.

generate $K_G(T)$. Computation of the generalized thermal load vector requires updating the physical thermal load vector and pre-multiplying by the modal matrix. Creation of the physical thermal load vector requires updating each element load vector based on the temperature change and assembling the global load vector. Because the number of physical degrees of freedom in the structural model is large, reassembling the physical stiffness matrix and thermal load vector at every aeroelastic time step within an aerothermoelastic simulation framework is undesirable. One goal of this paper is to examine techniques for reducing the computational cost of the structural ROM by avoiding the need to reassemble the physical stiffness matrix and thermal load vector at every time step. A method for directly updating the stiffness matrix and thermal loads based on a given temperature distribution is therefore under investigation to reduce the computational cost of the structural ROM. This can be seen as replacing the orange blocks in Fig. 1 with a reduced-order representation linking the transient thermal solution to the structural dynamic equations of motion. The generalized load vector due to aerodynamic loads, F_S^A, is still assembled in the usual manner as it only contains contributions to the loads at the outer surface of the structure and the associated computational cost is relatively low.

The methodology employed in this work is based on the kriging technique[36] which provides a global approximation to a function based on sampled training data. Kriging provides an approximation, $\hat{y}(b)$, to a function based on local deviations, $Z(b, X)$, from a global approximation, $R(b, X)$, of the form[37]

$$\hat{y}(b) = R(b, X) + Z(b, X), \tag{16}$$

where b is a vector of inputs corresponding to the untried location in the parameter space and X is a collection of the sample points used for the training data. The training response at the sample points is stored in the response matrix, $Y(X)$, such that

$$Y(X) = \begin{bmatrix} y_1^{(1)}\left(X^{(1)}\right) & y_1^{(2)}\left(X^{(2)}\right) & \dots & y_1^{(n_k)}\left(X^{(n_k)}\right) \\ y_2^{(1)}\left(X^{(1)}\right) & y_2^{(2)}\left(X^{(2)}\right) & \dots & y_1^{(n_k)}\left(X^{(n_k)}\right) \\ \vdots & \vdots & \ddots & \vdots \\ y_{n_p}^{(1)}\left(X^{(1)}\right) & y_{n_p}^{(2)}\left(X^{(2)}\right) & \dots & y_{n_p}^{(n_k)}\left(X^{(n_k)}\right) \end{bmatrix}, \tag{17}$$

where $y_i^{(j)}$ indicates the i-th entry of the response vector for the j-th kriging snapshot, $X^{(j)}$, n_k is the number of kriging snapshots, and n_p is the number of output parameters in a snapshot. The regression model $R(b, X)$ is an assumed function (usually of polynomial form), while $Z(b, X)$ is a realization of a stochastic process with zero mean, variance of σ^2, and non-zero covariance, and ensures that the kriging model interpolates the sampled data points exactly. Alternatively, $Z(b, X)$ represents uncertainty in the mean of $y(b)$ and the covariance matrix of $Z(b, X)$ for two points in the parameter space, $b^{(i)}$ and $b^{(j)}$, is given by

$$\text{Cov}\left[Z(b^{(i)}), Z(b^{(j)})\right] = \sigma^2 C[G(X^{(i)}, X^{(j)})], \tag{18}$$

where C is the correlation matrix that is assembled based on the chosen correlation function, $G(X^{(i)}, X^{(j)})$, and $X^{(i)}$ and $X^{(j)}$ are the i-th and j-th sample points, respectively. In Eq. (18), the process variance, σ^2,

functions as a scale factor that can be tuned to the training data. The role of the correlation function is to account for the effect of each interpolation point on every other interpolation point and quantifies how quickly and smoothly the function moves from point $X^{(i)}$ to point $X^{(j)}$. In this work, a Gaussian correlation function is used, and is given by[37]

$$G(X^{(i)}, X^{(j)}) = \exp\left[-\sum_{k=1}^{n_{dv}} \theta_k \left|X_k^{(i)} - X_k^{(j)}\right|^{p_k}\right], \tag{19}$$

where n_{dv} is the number of design variables or parameters, θ_k and p_k are the unknown fitting parameters, and $X_k^{(i)}$ denotes the k-th component of the i-th sample point. The bounds on the fitting parameters are: $\theta_k > 0$ and $0 < p_k \leq 2$. As the point $X^{(i)}$ approaches $X^{(j)}$, Eq. (19) approaches its maximum value of one, leading to the property that the kriging surface passes through the sampled data points. Therefore, the Gaussian correlation function is intuitive in that the closer two points become in the parameter space, the greater the correlation between the two points becomes. The parameters θ_k in Eq. (19) serve to provide a measure of activity in the variable X_k. Large values of θ indicate that there is strong correlation only for sample points that are close together. Small values of θ indicate that sample points points spaced further apart still have a strong influence on each other because they are well correlated. An alternative interpretation of the θ_k parameters is associated with dependence of the function on the k-th design variable. If the k-th design variable is active, there exist large differences in the function values at $X_k^{(i)}$ and $X_k^{(j)}$. Thus, the corresponding θ_k parameter will be large such that even though the absolute difference between $X_k^{(i)}$ and $X_k^{(j)}$ is small, the correlation between the function values at the i-th and j-th snapshot is low due to the fact that it changes rapidly with changes in the k-th design variable. The exponents p_k are related to the smoothness of the function of interest in the direction of the k-th design variable, with increasing p_k corresponding to increasing smoothness. In order to determine the fitting parameters, the form of $R(b, x)$ must first be chosen.

To derive the prediction equations, a vector containing the regression functions, denoted by r_x, is assembled such that

$$R(b, X) = r_x^T \beta, \tag{20}$$

where r_x^T is a $1 \times n_b$ row vector of basis functions with n_b being the number of basis functions associated with the regression polynomial, and β is an $n_b \times 1$ column vector of coefficients of each of the polynomial terms. The expanded design matrix, R_x, is of the form[38]

$$R_x(X) = \begin{bmatrix} r_x^T(X^{(1)}) \\ r_x^T(X^{(2)}) \\ \vdots \\ r_x^T(X^{(n_k)}) \end{bmatrix}, \tag{21}$$

such that i-th row of R_x corresponds to the evaluation of the n_b basis functions at the i-th kriging snapshot. If the stochastic process evaluated at the kriging snapshot points is denoted as

$$z(X) = \left[Z(X^{(1)}), Z(X^{(2)}), \ldots, Z(X^{(n_k)})\right]^T \tag{22}$$

then the training data can be represented as

$$Y(X) = R_x \beta + z. \tag{23}$$

The goal of the kriging methodology is to obtain the best linear unbiased predictor, where unbiasedness refers to the fact that the expected value of the predictor must be equal to the expected value of Eq. (23). This is accomplished by solving an optimization problem to minimize the error of the predictor subjected to constraints that ensure unbiasedness. This procedure results in the kriging predictor being given by

$$\hat{y}(b) = r_x^T \hat{\beta} + g^T(b, X) G^{-1} \left(y - R_x \hat{\beta}\right), \tag{24}$$

where y is a column vector of length n_k containing the values of the function outputs at the sample points and $g^T(b, X)$ is a correlation vector between the untried point, b, and the sample data points, X, such that

$$g(b, X) = \left[G(b, X^{(1)}), G(b, X^{(2)}), \ldots, G(b, X^{(n_k)})\right]^T. \tag{25}$$

In Eq. (24), $\hat{\beta}$ is the generalized least squares estimator of β and is given by

$$\hat{\beta} = \left(R_x^T C^{-1} R_x\right)^{-1} R_x^T C^{-1} y. \tag{26}$$

At this point, it remains to determine the fitting parameters θ_k and p_k in Eq. (19). As the stochastic process associated with the error of the kriging regressors is assumed to be Gaussian, the optimal values of θ_k and p_k are those that maximize the likelihood that the interpolation points have been drawn from such a process. Alternatively stated, we seek to choose θ_k and p_k leading to a kriging function such that the consistency between the actual model and the kriging predictions of the model is maximized. The problem of obtaining the maximum likelihood estimates of θ_k and p_k is posed as

$$\min_{\theta_k>0,\ 0<p_k\leq 2} -\frac{n_k \ln\left(\hat{\sigma}^2\right) + \ln|C|}{2}, \tag{27}$$

where $|C|$ is the determinant of C and $\hat{\sigma}$ is the generalized least squares estimate of σ given by

$$\hat{\sigma}^2 = \frac{\left(y - R_x\hat{\beta}\right)^T C^{-1} \left(y - R_x\hat{\beta}\right)}{n_k}. \tag{28}$$

The maximum likelihood estimate given in Eq. (27) is a function of the θ_k and p_k parameters only, and one can thus utilize nonlinear optimization techniques to obtain these parameters. While any values of θ_k and p_k would result in a kriging model that interpolates the sample points exactly, the "best" kriging model is that which utilizes those values of θ_k and p_k which minimize the function given in Eq. (27).

VII.B. Use of Kriging for Efficient Update of Stiffness and Thermal Loads

In this application the quantities to be approximated using kriging, $\hat{y}$, are the entries of the stiffness matrix and the thermal load vector, and the inputs to function, b, are spatially varying temperature distributions. Because the current full-order thermal model contains 2,812 degrees of freedom, it is impractical to treat each thermal degree of freedom as a variable in the parameter space. This is due to the fact that the resulting parameter space would be too large to realistically sample when generating the kriging training data. However, as POD is already being used for the thermal ROM, it provides a convenient and optimal means for parameterizing the transient temperature distribution in terms of a small number of variables. By using the truncated set of thermal POD modal coordinates as the parameters to represent the complete temperature distribution, the number of parameters to be sampled is greatly reduced. The large-scale reduction in the number of design variables needed to represent the physical temperature distribution is due to the optimality of the POD basis. Recall that the POD basis is optimal in the sense that it captures the solution more accurately in a finite number of modes than any other basis representation using the same number of modes, provided that the POD snapshots adequately capture the dynamics of the system. This optimality is critical as the computational effort required to construct a kriging model is a strong function of the number of design variables involved.

Because of the large number of structural degrees of freedom, the computational cost and memory associated with updating the physical stiffness matrix, $K_S^*(T)$, and pre- and post-multiplying by the structural reference modes at every aeroelastic time step is undesirable. As such, kriging is used to directly create the generalized stiffness matrix, $k_S^*(T)$, which is of reduced size and does not possess the computational issues associated with the physical stiffness matrix. As the number of entries in the physical thermal load vector, F_S^H, is reasonable, error analysis is conducted on kriging models for both the physical and generalized thermal load vectors to assess which one can be more accurately represented.

The first step in the process is to generate the thermal POD vectors to be used in parameterizing the transient temperature distribution. To accomplish this, an aerothermoelastic simulation is run for a time-history of one hour at $M = 8$, $h = 26$ km, $\alpha = 3°$, and a uniform initial temperature distribution, T_0, of 293 K. In a previous work by the authors[14] it was found that there is a steep initial temperature gradient as the structure begins heating up, and the maximum temperature increases until approximately 150 s into the transient, at which point it begins to reach a steady state. As such, two different sets of time steps are used to adequately capture the dynamics of the thermal system. For the period from 0 – 150 s, the time steps are chosen as follows: $\Delta t_{HT} = \Delta t_{AE} = 0.1$ s, and $\Delta t_{AT} = 1$ s. For the period from 150 s – 3,600 s,

the time steps are chosen as follows: $\Delta t_{HT} = \Delta t_{AE} = 1$ s, and $\Delta t_{AT} = 5$ s. The goal of using smaller time steps initially is to provide more resolution for the period in which the dynamics of the thermal system are changing on a faster time scale. One thermal snapshot is taken at each heat transfer time step regardless of the size of the time step, resulting in a total of 4,951 snapshots.

After the snapshot matrix is assembled, its singular value decomposition is taken in order to generate the POD basis vectors. The eigenvalues of the correlation matrix are computed based on the singular values and are used to assess the relative contribution of each POD mode. The first 24 eigenvalues of the correlation matrix are shown in Fig. 16. The retained POD modes are chosen by selecting those modes whose corresponding eigenvalue is greater than one. Based on this criteria, the first 15 POD modes are retained. The fact that the POD modal truncation results in a set of 15 modes being retained is advantageous in that the number of design variables involved in the kriging training procedure has now been reduced to a feasible level.

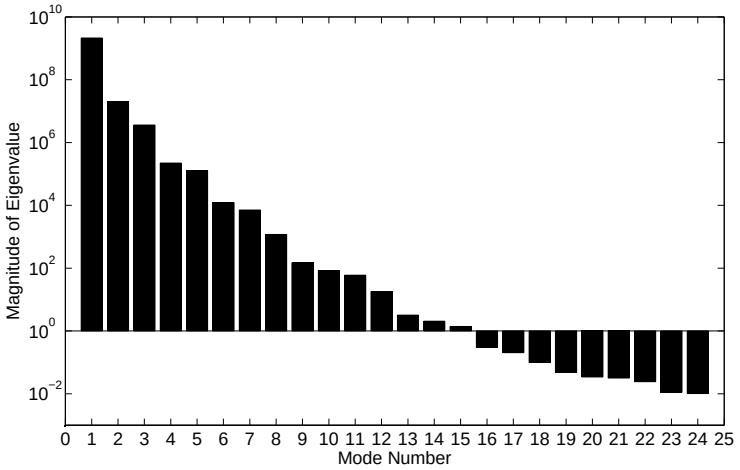

Figure 16. Semi-log plot of first 24 eigenvalues of correlation matrix.

With the design variables chosen, the next step of the process is to generate the kriging sample points to be used in construction of the ROM. This is accomplished using the LHS methodology. In this case, each kriging sample point consists of a set of 15 POD modal coordinates. Before the sample points can be generated, upper and lower bounds must be established for each design variable. This is accomplished by first calculating the vector of POD modal coordinates for each thermal snapshot based on the chosen POD basis by solving for c in the equation

$$\bar{\Phi}_T c = T, \tag{29}$$

where $\bar{\Phi}_T$ is the matrix containing the truncated set of POD modes, c is the vector of modal coordinates to be found, and T is a vector of temperatures corresponding to a given snapshot. Because there are more equations than unknowns in Eq. (29), c is computed in the least squares sense. Once c is known for each thermal snapshot, an interval is found for each modal coordinate by subtracting the minimum value of each modal coordinate from the corresponding maximum value. Because these intervals corresponds to the specific flight conditions at which the thermal POD snapshots were taken, they may not encompass the full range that the POD modal coordinates can assume across the full spectrum of flight conditions. In order to account for variability in the POD modal coordinates with flight conditions and boundary conditions, the interval size for each POD modal coordinate is multipled by a factor of three by increasing each upper bound and decreasing each lower bound by equal amounts.

With the upper and lower bounds for each modal coordinate established, the LHS methodology is used to generate the kriging sample points. Because the sampling is performed on the POD modal coordinates and not on the nodal temperatures themselves, the resulting temperature vector may be out of the expected range for the structure for certain combinations of POD modal coordinates. To account for this, bounds are also established on minimum and maximum allowable values of the resulting nodal temperatures. After the sample points are generated, the temperature vector corresponding to each sample point is found using the chosen POD basis. A filtering process is then employed that eliminates sample points whose corresponding minimum and maximum nodal temperature values lie outside the range of 293 K – 1,500 K. It is therefore

necessary to generate more sample points than desired as not all sample points will be accepted.

Once the inputs for each training run are generated, high-fidelity analysis is conducted to generate the training data for each sample point. This step consists of generating the temperature distribution corresponding to the selected POD modal coordinates and computing the resulting stiffness matrix and thermal load vector at that temperature distribution. The generalized stiffness matrix calculation is performed by assembling the physical stiffness matrix and pre- and post-multiplying by the chosen structural reference modes. The physical stiffness matrix is computed using Eq. (7) and contains contributions from both the conventional stiffness matrix with temperature-dependent material properties, $K_S(T)$, and the geometric stiffness resulting from thermal stresses, $K_G(T)$. The assembling of the matrices and vectors required for the kriging training process is accomplished via the use of Nastran DMAP. For this case, the structural reference modes are chosen to be the first ten free vibration modes at the reference thermal state. The reference thermal state is obtained by averaging the 4,951 thermal snapshots used in generating the POD basis. Because the kriging ROM is necessary to evaluate the accuracy of the structural basis, the validity of this structural basis is not studied in the current section. It is used simply as a placeholder at this stage for the purpose of evaluating the accuracy of the kriging ROM with a fixed structural basis. Subsequent sections will provide detailed examination of selection of a robust structural basis.

Using the set of sample points along with the output data, kriging surrogates are created for the stiffness matrix and thermal loads using a second order polynomial regression model. Once the kriging models are generated, the errors associated with each are quantified. If the accuracy of the models is acceptable, they can then be used within the aerothermoelastic simulation framework. If greater accuracy is desired, more sample points are added and the kriging models are updated. The procedure for error quantification is based on that utilized by Crowell et al.[23] The process involves first generating an independent set of evaluation points using LHS. Again, these evaluation points are subjected to the criteria that they must generate nodal temperatures that lie within the range 293 K – 1,500 K. The number of kriging evaluation points, n_e, is chosen to be 500 in this work. For each evaluation point, the stiffness matrix and thermal load vector are calculated using both the full-order model and the kriging ROM. To quantify the error between the full-order and kriging solutions, two different error metrics are utilized. The first error metric is the normalized root mean squared error (NRMSE). Expressed as a percentage, the NRMSE is given by

$$\text{NRMSE} = \frac{\sqrt{\frac{1}{q}\sum_{i=1}^{q}\left(\text{ROM}_i - \text{Full}_i\right)^2}}{\text{Max(Full)} - \text{Min(Full)}} \times 100\%, \tag{30}$$

where i is the i-th output quantity, "ROM" represents a solution vector of the reduced-order model, "Full" represents a solution vector of the full-order model, and q is the total number of output quantities. Also, note that "Max" and "Min" correspond to the maximum and minimum entries, respectively, of the vector of interest. The output quantities are the entries of the generalized stiffness matrix and the physical or generalized thermal load vector, and thus i is summed over all of the entries of the vector of interest in the numerator of Eq. (30). Note that the generalized stiffness matrix is reshaped into a column vector for the purpose of error analysis. The second error metric utilized is the L_∞ error. Expressed as a percentage, the L_∞ error is given by

$$L_\infty = \frac{\text{Max}\left(|\text{ROM} - \text{Full}|\right)}{\text{Max(Full)} - \text{Min(Full)}} \times 100\%. \tag{31}$$

Note that the error metrics are calculated for each evaluation case. To determine a scalar measure of error for the ROMs, both the average and maximum values of the NRMSE and L_∞ error over all evaluation cases are examined.

To examine the error of the kriging ROMs as a function of number of sample points, kriging models for both the generalized stiffness matrix and generalized thermal load vector are generated using varying numbers of sample points. Two different criteria are utilized in generating the set of Latin Hypercube sample points. The first, denoted "maximin", aims to maximize the minimum distance between sample points over a specified number of iterations. The second, denoted "correlation", aims to minimize the correlation between sample points over a specified number of iterations. In both cases, the maximum allowable number of iterations is set to 500. The error metrics are computed for each kriging ROM over 500 evaluation snapshots which are always generated using the "maximin" criterion over 500 iterations. Plots of the average NRMSE and L_∞ error for the generalized stiffness ROM as a function of number of sample points are given in Fig. 17(a) and Fig. 17(b), respectively, using both the "maximin" and "correlation" criteria. Similarly, plots

of the average error for the generalized thermal load vector ROM are given in Fig. 18(a) and Fig. 18(b), respectively, using both the "maximin" and "correlation" criteria. Due to memory requirements associated with the "maximin" criterion, the maximum number of sample points used with this criterion is 3,000, while up to 6,000 are taken for the "correlation" cases. As seen in the figures, there is not a significant difference between the results obtained using the "maximin" criterion and the "correlation" criterion. Due to the higher computational cost and memory requirements associated with the "maximin" criterion, the "correlation" criterion with a maximum of 500 iterations is used from this point forward. Comparing Fig. 17 with Fig. 18, it is evident that generalized stiffness matrix ROM is significantly more accurate than the generalized thermal load vector ROM for the same number of snapshots.

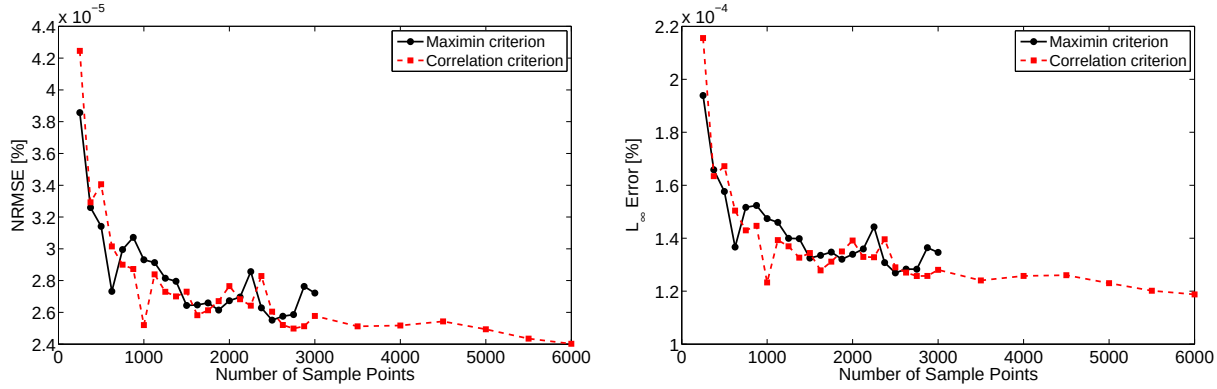

(a) Average NRMSE.

(b) Average L_∞ Error.

Figure 17. Average errors for generalized stiffness matrix ROM over 500 evaluation cases.

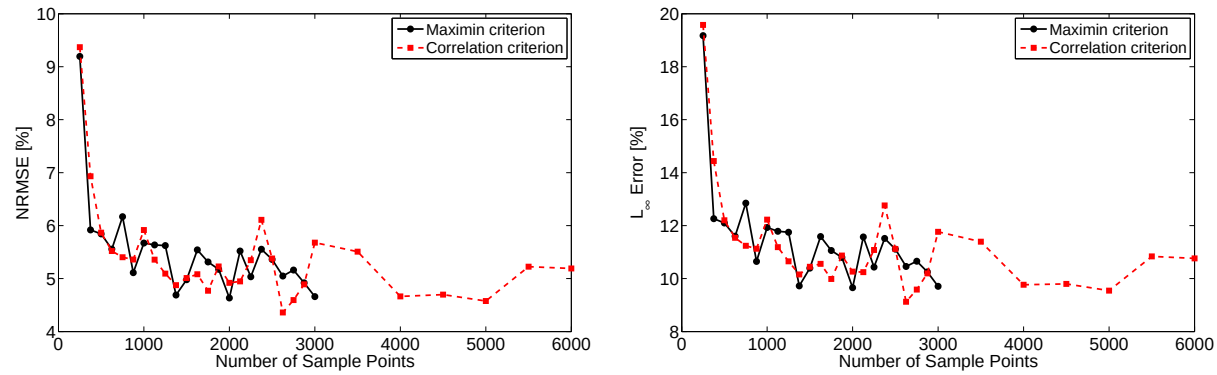

(a) Average NRMSE.

(b) Average L_∞ Error.

Figure 18. Average errors for generalized thermal load vector ROM over 500 evaluation cases.

To understand why the error of the generalized stiffness ROM is significantly lower than that of the generalized thermal load vector ROM, the functional dependence of the generalized stiffness matrix on the POD modal coordinates is examined. Recall that the physical stiffness matrix is the sum of the conventional stiffness matrix and geometric stiffness matrix, i.e.

$$K_S^*(T) \equiv K_S(T) + K_G(T). \tag{32}$$

The entries of the generalized stiffness matrix are simply linear combinations of the entries of the physical stiffness matrix and do not affect the order of its dependence on temperature. The dependence of $K_S(T)$ and $K_G(T)$ on the POD modal coordinates is through the variation of material properties with temperature. The entries of the conventional stiffness matrix, $K_S(T)$, are only dependent on the Young's modulus of the corresponding material, i.e.

$$K_{S,i} \propto E(T_i), \tag{33}$$

where i denotes a particular degree of freedom. The entries of the geometric stiffness matrix, $K_G(T)$ are dependent on the Young's modulus, coefficient of thermal expansion, and temperature change, i.e.

$$K_{G,i} \propto E(T_i), \alpha_T(T_i), \Delta T_i, \tag{34}$$

where the temperature is always expressed as a linear combination of the POD basis vectors such that

$$T_i = \sum_{j=1}^{r} c_j \varphi_i^{(j)}, \tag{35}$$

where r is again the number of degrees of freedom in the reduced-order thermal model. In order to understand the order of the functional dependence the entries of $K_S(T)$ and $K_G(T)$ on the POD modal coordinates, c_j, it is first necessary to know the order of the functional dependence of E and α_T on temperature for each material in the model. This information is given in Table 2 for each of the three materials used in the model, where each entry in the table gives the order of the polynomial representing the temperature-dependence of the material preoperty. Recall that the stiffness and thermal expansion of the insulation layer are neglected in the structural model.

Table 2. Orders of dependence of E and α_T on temperature.

	$E(T)$	$\alpha_T(T)$
Heat Shield (René 41)	Quadratic	Cubic
Insulation (Min-K)	N/A	N/A
Skin/Stiffeners (TIMETAL834)	Linear	Constant

Based on the information given in Table 2, the entries of $K_S(T)$ can depend on at most the second power of c_j, and the entries of $K_G(T)$ can depend on at most the sixth power of c_j. Because the regression model used for the kriging function is quadratic, one would expect the generalized stiffness matrix to be well approximated by the kriging model if the generalized stiffness was at most a quadratic function of the POD modal coordinates. Thus, one potential reason that the kriging representation of the generalized stiffness matrix is of such high accuracy is that $K_S(T)$ is dominant over $K_G(T)$, and that $K_S^*(T)$ is essentially quadratic in T with small perturbations due to geometric stiffening. To examine this hypothesis, the relative magnitudes of $K_S(T)$ and $K_G(T)$ are assessed as a function of temperature. The temperature is varied by holding all modal coordinates constant except for the first, and increasing c_1 linearly. For each increment of c_1, the Frobenius norms of both $K_S(T)$ and $K_G(T)$ are computed in order quantify the relative magnitude of each. Plots of the Frobenius norms of $K_S(T)$ and $K_G(T)$ as a function of c_1 are given in Fig. 19(a) and Fig. 19(b), respectively. Comparing the two plots, $K_S(T)$ is approximately three orders of magnitude larger than $K_G(T)$ based on the chosen norm. This indicates that the generalized stiffness matrix is essentially quadratic in the POD modal coordinates with small perturbations due to geometric stiffening. Because the regression model used for the kriging ROM of the generalized stiffness matrix is also quadratic, the errors associated with the generalized stiffness matrix ROM are low.

Though the average NRMSE of the generalized thermal load vector remains below 10% as shown in Fig. 18(a), higher accuracy for the thermal loads is still desired. One potential means for improving the representation of the thermal loads is to perform the kriging interpolation on the physical thermal load vector, F_S^H, as opposed to the generalized thermal load vector, f_S^H. Because the number of entries in the physical thermal load vector is at a feasible level (8,074), memory and computational cost issues will not come into play as they would in the case of the physical stiffness matrix. To investigate the ability of kriging to capture the entries of the physical thermal load vector, the same error analysis as used for the generalized thermal load vector is repeated on the physical one. The "correlation" criterion with a maximum of 500 iterations is again used to generate the sample points for the training data. Plots of the average NRMSE and L_∞ error over the evaluation cases are given in Fig. 20(a) and Fig. 20(b), respectively.

Comparing Fig. 20 to Fig. 18, it is observed that greater accuracy can be obtained by performing the kriging interpolation on the physical thermal load vector instead of the generalized thermal load vector. To understand why this is the case, first consider the dependence of the entries of the physical load vector on temperature. The physical thermal load vector is proportional to the Young's Modulus, coefficient of

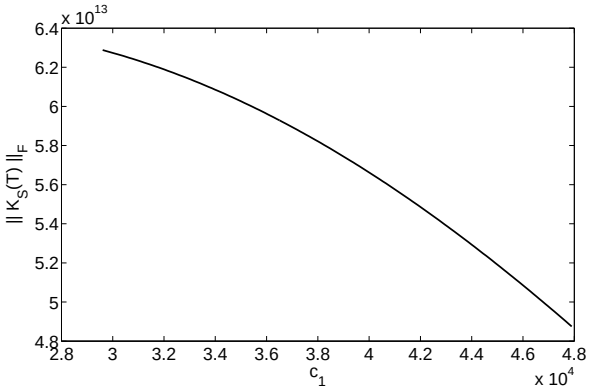

(a) Norm of $K_S(T)$.

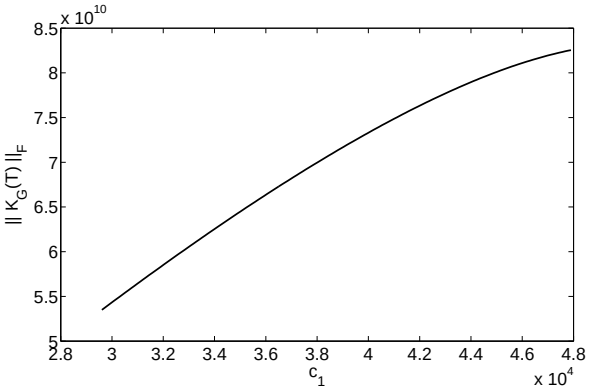

(b) Norm of $K_G(T)$.

Figure 19. Frobenius norms of the conventional and geometric stiffness matrices as a function of the first POD modal coordinate.

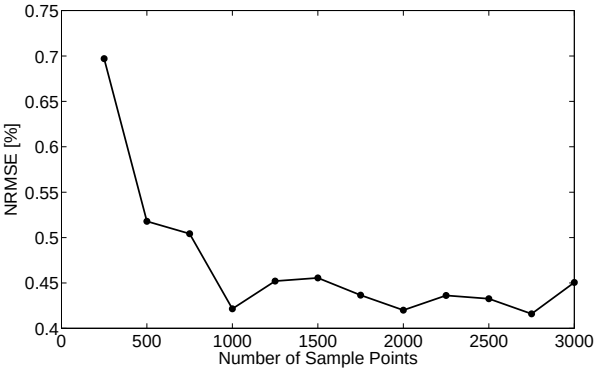

(a) Average NRMSE.

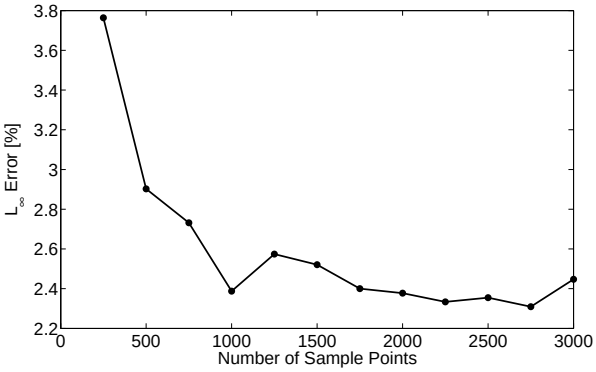

(b) Average L_∞ Error.

Figure 20. Average errors for physical thermal load vector ROM over 500 evaluation cases.

thermal expansion, and change in temperature, i.e.

$$F_{S,i}^{H} \propto E(T_i), \alpha_T(T_i), \Delta T_i, \quad \text{where } T_i = \sum_{j=1}^{r} c_j \varphi_i^{(j)}. \tag{36}$$

Based on the information presented in Table 2, this means that the physical thermal load vector depends on the second power of c for skin and stiffener elements and the sixth power of c for heat shield elements. In order to compute the generalized thermal load vector, inner products between the structural modes and the physical thermal load vector are required. The i-th entry of the generalized thermal load vector is given by

$$f_{S,i}^{H} = \sum_{l=1}^{s} \phi_l^{(i)} F_{S,l}^{H}, \tag{37}$$

where $\phi_l^{(i)}$ denotes the l-th entry of the i-th structural reference mode and s is the total number of degrees of freedom in the structural model (8,074 in this case). Whereas as the physical thermal load vector depends on the second power of c for skin and stiffener elements and the sixth power of c for heat shield elements, the generalized thermal load vector depends on the sixth power of c for all elements because it is summed over all entries of F_S^H. Therefore, the generalized thermal load vector is a more complex function of the POD modal coordinates than the physical one. The only caveat associated with using kriging to generate the physical load vector is that the physical thermal load vector must be pre-multiplied by the structural reference modes each time it is updated in order to transform to modal space. However, the computation time involved in transforming the loads from physical space to modal space is expected to be minimal. Thus, the physical thermal load vector and not the generalized thermal load vector will be approximated with kriging in this work.

Though the accuracy of the generalized stiffness matrix and physical thermal load vector ROMs appear sufficient based on the NRMSE and L_∞ plots given in Fig. 17 and Fig. 20, recall that these results are obtained by averaging the error metrics over 500 evaluation cases. As one of the objectives of this study is to bound the error of the kriging ROMs, it is necessary to investigate the worst-case error over the parameter space. As such, the maximum L_∞ error over the 500 evaluation cases is plotted for both the generalized stiffness matrix ROM and the physical thermal load vector ROM as a function of number of sample points. This metric gives the worst-case error over all degrees of freedom over all evaluation cases. Results are given in Fig. 21(a) and Fig. 21(b). Comparing the two figures, the worst-case error of the physical thermal load vector ROM is several orders of magnitude higher than that of the generalized stiffness matrix ROM. As it is desirable to reduce the worst-case error of the physical thermal load vector ROM, further investigation into the source of the higher errors is warranted. To give an indication of the spatial variation of the error, a new error metric, denoted by ϵ, is introduced. This error metric corresponds to the percentage error for each degree of freedom and given by

$$\epsilon_i = \frac{|\text{ROM}_i - \text{Full}_i|}{\text{Full}_i} \times 100\%, \tag{38}$$

where i denotes the i-th degree of freedom. In order to determine the sources of error for the physical thermal load vector ROM, it is necessary to determine which degrees of freedom generally show the largest discrepancy between thermal loads calculated by the full-order model and those predicted by the kriging model. To accomplish this, the degree of freedom number at which the maximum value of ϵ occurs for the physical thermal load vector ROM is recorded for each evaluation case. The number of times that the maximum percentage error occurs at each degree of freedom is then summed and plotted as a function of degree of freedom in Fig. 22 for the physical thermal load vector ROM generated using 3,000 sample points. Note that the skin and stiffener elements correspond to degrees of freedom 1–2752, and the heat shield elements correspond to degrees of freedom 2753–8,074. Examining Fig. 22, in can be observed that the maximum percentage error generally occurs at those degrees of freedom corresponding to the heat shield. This is expected as the thermal loads for the heat shield are a higher order function of temperature than the thermal loads for the skin and stiffeners.

Due to the higher order dependence of the heat shield thermal loads on temperature, it is expected that the use of a higher order regression model will improve the accuracy of the representation of the thermal loads. To examine this hypothesis, a third-order regression model was implemented for comparison against

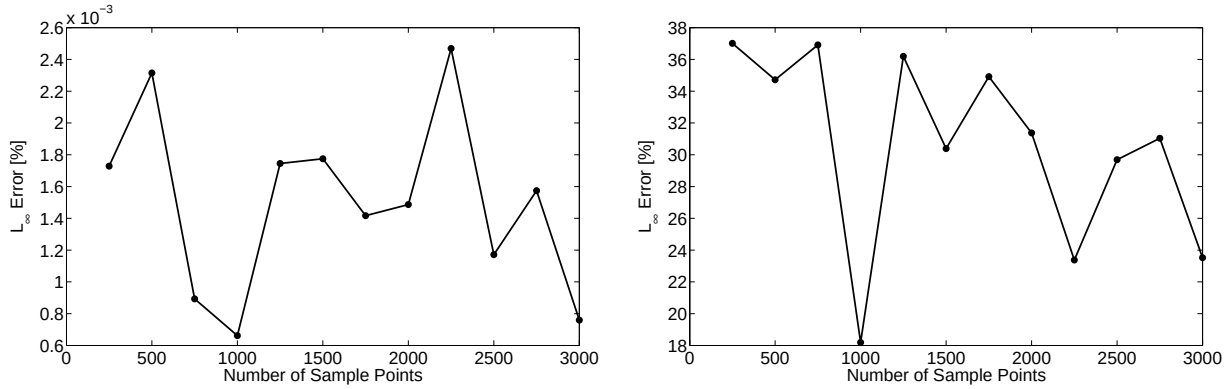

(a) Generalized stiffness matrix ROM.

(b) Physical thermal load vector ROM.

Figure 21. Maximum L_∞ errors over 500 evaluation cases for kriging ROMs of $k_S^*(T)$ and $F_S^H(T)$ using 2nd order regression model.

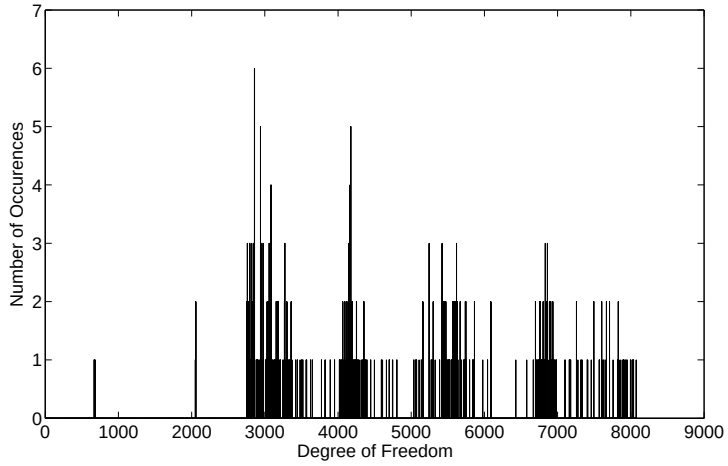

Figure 22. Number of occurrences of maximum percentage error at each degree of freedom for physical thermal load vector ROM generated using 3,000 sample points.

the results obtained using the second-order regression model. The maximum L_∞ error of the physical thermal load vector ROM over 500 evaluation cases is plotted as a function of number of sample points for both the second-order and third-order regression models as shown in Fig. 23. The figure shows significant improvement in capturing the thermal loads by moving from a second-order regression function to a third-order regression function. It is observed that for the third-order regression function, all data points remain at or below 5% maximum L_∞ error over the evaluation cases.

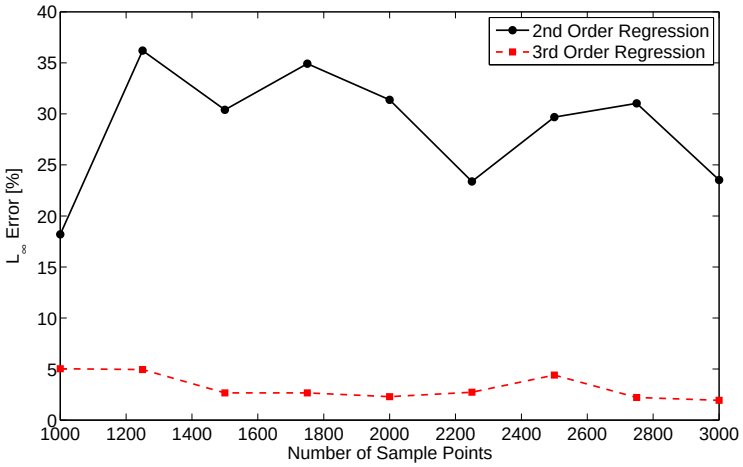

Figure 23. Maximum L_∞ error over 500 evaluation cases for kriging ROMs of $F_S^H(T)$ using both 2nd and 3rd order regression models.

Note that the minimum number of sample points used in Fig. 23 is 1,000. This is due to the fact that there is a minimum bound on the number of sample points used to create the kriging ROM based on the number of basis functions, n_b, required by the regression model. In order to ensure that the problem is not under-constrained, the number of sample points used in creating the kriging ROM, must be equal to or greater than the number of basis functions in the regression model, i.e. $n_k \geq n_b$. Therefore, the order of the regression model must not be chosen to be arbitrarily high as there is a trade-off between the order of regression and the minimum number of required sample points. The number of basis terms, and thus the minimum number of required sample points, is given by

$$n_b = \frac{\prod_{i=1}^{\mathcal{O}} (n_{dv} + i)}{\mathcal{O}!}, \tag{39}$$

where $\mathcal{O}$ is the order of the regression model. For the current case in which 15 design variables are considered, n_b is 120 for a second-order regression model, 816 for a third-order regression model, and 3,876 for a fourth-order regression model. Thus, care must be taken when selecting the order of regression and number of design variables to consider as there exists an important trade-off between the accuracy of the kriging ROM, the computational expense required to create the kriging ROM, and the number of design variables included.

VII.B.1. Methodology for Bounding POD Modal Coordinates

For the kriging results presented thus far, the bounds on the POD modal coordinates were established based on the maximum and minimum values of each for a single full-order aerothermoelastic simulation under one specific set of flight conditions. If the POD modal coordinates remain within these bounds throughout the simulations in which the kriging ROMs are used, the discussion of kriging error presented above is valid. However, there is no guarantee of accuracy if the POD modal coordinates go outside of the bounds which were used in generating the training data. As such, a robust and efficient method for bounding the POD modal coordinates is developed. An overview of the proposed methodology is given in Fig. 24.

The process begins by identifying the range of flight conditions for which the kriging ROMs are to be valid for. The flight conditions of interest are the Mach number, angle of attack, and altitude. Using the bounds on the flight conditions, the LHS procedure is used to generate n flight condition sets. One of the sample points must correspond to the highest dynamic pressure case (maximum Mach number, maximum angle of

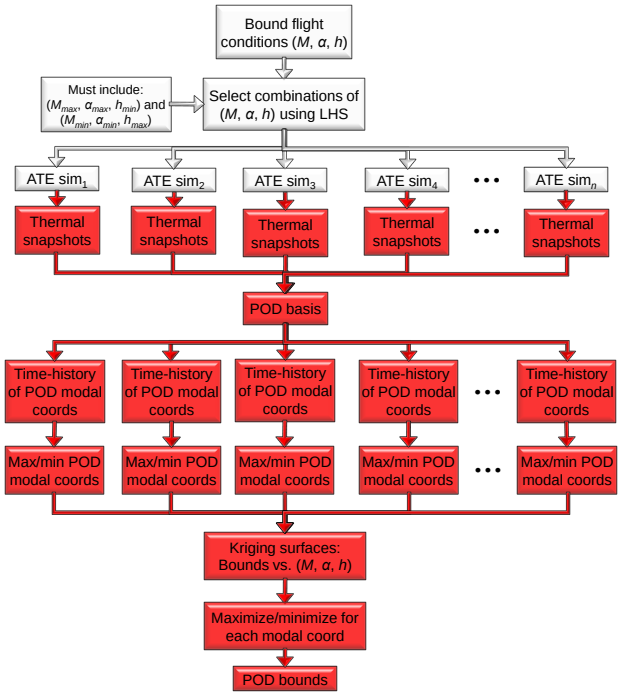

Figure 24. Proposed methodology for generating thermal snapshots and bounding POD modal coordinates.

attack, and minimum altitude), and another sample point must correspond to the lowest dynamic pressure case (minimum Mach number, minimum angle of attack, and maximum altitude). For each set of flight conditions, a full-order aerothermoelastic simulation is carried out and thermal snapshots are taken. Note that these simulations are performed in parallel such that the time to generate all of the thermal snapshots is the computation time for a single full-order simulation. Once the thermal snapshots are obtained from all of the full-order aerothermoelastic simulations, they are combined into a single snapshot matrix and the POD basis is generated. The POD basis is then used along with the snapshots to calculate what the time-history of the POD modal coordinates would have been had the thermal ROM been used for each set of flight conditions. For each case, the maximum and minimum values of each POD modal coordinate are identified, and this information is used to create a kriging surface that gives the bounds on each of the POD modal coordinates as a function of the Mach number, angle of attack, and altitude. This kriging surface is then used as a surrogate model for the purpose of finding the maximum possible upper bound and minimum possible lower bound for each POD modal coordinate at any location within the parameter space of the flight conditions. Once the POD bounds are established, they are used in the generation of sample points for the kriging ROMs of the stiffness matrix and thermal load vector. This framework serves two important purposes. In addition to providing robust bounds on the POD modal coordinates, the framework also leads to the generation of a rich set of thermal snapshots, leading to an accurate thermal POD model.

One challenge involved in bounding the POD modal coordinates is associated with their initial conditions. If the relations given in Eq. (4) are solved directly for the POD modal coordinates, it is likely that the bounds will be exceeded for simulations whose initial conditions vary from those at which the bounds were generated. It is therefore desirable to generate bounds that are independent of the initial conditions by transforming Eq. (3) such that the initial conditions are made to be uniform and homogeneous. This is accomplished by defining a new variable, $\tilde{T}$, which represents the excess of temperature over the initial condition, i.e.,

$$\tilde{T}(t) = T(t) - T_0, \tag{40}$$

where T_0 is the vector of initial temperatures. Applying this transformation to Eq. 3, the system becomes

$$M\dot{\tilde{T}}(t) + K\tilde{T}(t) = G_T(t), \tag{41}$$

where $G_T(t) = F(t) - KT_0$. As before, the system is transformed to modal space using

$$\bar{\Phi}_T^T M_T \bar{\Phi}_T \dot{\tilde{c}}(t) + \bar{\Phi}_T^T K_T \bar{\Phi}_T \tilde{c}(t) = \bar{\Phi}_T^T G_T(t), \tag{42}$$

where $\tilde{c}$ denotes the fact that the system has been transformed to impose homogeneous initial conditions. Once the system is solved for $\tilde{c}(t)$, the physical temperatures are obtained by multiplying the POD basis with the POD modal coordinates and adding the initial conditions back on, i.e.

$$T(t) = \bar{\Phi}\tilde{c}(t) + T_0. \tag{43}$$

In addition to making the bounds independent of the initial conditions, this transformation provides another benefit in terms of improving the accuracy of the thermal ROM. If the initial conditions were not made to be homogeneous, the initial value of each POD modal coordinate would be found by projecting T_0 in the direction of the corresponding POD basis vector, i.e.,

$$c_i(0) = \left\langle \varphi^{(i)}, T_0 \right\rangle, \tag{44}$$

where $\langle\cdot\rangle$ denotes an inner product. Because the POD basis does not form a complete space for the physical temperatures, the initial temperature distribution cannot be represented exactly in this formulation. However, by transforming the equations to enforce homogeneous initial conditions, $\tilde{c}(0)$ is forced to become a vector of zeros and $T(t)$ can be represented exactly after the vector of initial conditions is added back to the solution. For the current framework in which Eq. (42) is integrated numerically and the solution at each time step depends on that at the previous time step, the ability to represent the initial conditions exactly is important.

In order to account for the transformation of Eq. (40) in the kriging representation of the stiffness matrix and thermal loads, additional design variables corresponding to T_0 must be included in the kriging functions. This is necessary because the design variables passed to the kriging functions must be capable of reproducing the physical temperature distribution including the effect of the initial condition. In this work the initial temperature distribution is assumed to always be uniform such that the physical temperature distribution can be expressed as

$$T(t) = \left[\sum_{i=1}^{r} c_i(t)\varphi^{(i)}\right] + \mathcal{T}_0\{\mathbf{1}\}, \tag{45}$$

where $\mathcal{T}_0$ is the scalar value of the uniform initial temperature and $\{\mathbf{1}\}$ is a vector of ones of length s. Thus the design variables for the kriging ROMS are the POD modal coordinates, c_i, and the scalar value of the initial temperature, $\mathcal{T}_0$. Because the initial condition is taken to be uniform here, only one additional design variable is required to represent the initial condition. Arbitrary spatial variation of the initial conditions can be permitted by replacing $\mathcal{T}_0\{\mathbf{1}\}$ in the right-hand side of Eq. (45) with a linear combination of multiple basis vectors. Note that this would require a larger number of design variables to represent the initial conditions.

The framework of Fig. 24 is implemented for the ranges in flight conditions shown in Table 3. Ten sets of flight conditions are identified using LHS. As before, two different sets of time step sizes are used in the aerothermoelastic simulations. For the period 0 – 150 s, the time step sizes are: $\Delta t_{HT} = \Delta t_{AE} = 0.1$ s, and $\Delta t_{AT} = 1$ s. For the period from 150 s – 3,600 s, the time step sizes are: $\Delta t_{HT} = \Delta t_{AE} = 1$ s, and $\Delta t_{AT} = 5$ s. One thermal snapshot is taken at each heat transfer time step. This results in total of 4,951 snapshots for each of the ten full-order aerothermoelastic simulations, and thus a total of 49,510 snapshots are used in the generation of the POD basis.

Table 3. Bounds on flight conditions for kriging ROM generation.

5.0	$\leq$	M_∞	$\leq$	8.0
0.0°	$\leq$	α	$\leq$	4.0°
25.0 km	$\leq$	h	$\leq$	45.0 km
293 K	$\leq$	$\mathcal{T}_0$	$\leq$	1500 K

Using the 49,510 snapshots obtained from the ten full-order aerothermoelastic simulations, the POD basis is generated. The eigenvalues associated with the first 50 POD modes are given in Fig. 25. The criterion used in the basis truncation process is to retain all POD vectors whose corresponding eigenvalue is greater than or equal to one. Thus, 32 POD vectors are retained after basis truncation in this case. Though the thermal ROM is not the focus of this paper, its accuracy is assessed for one set of flight conditions. The flight conditions used for verifying the accuracy of the POD basis are as follows: $M_\infty = 6.5$, $\alpha = 2°$, and $h = 35$

km. The time steps for this case are: $\Delta t_{AE} = \Delta t_{HT} = 0.1$ s, and $\Delta t_{AT} = 1$ s. The NRMSE and L_∞ error of the thermal ROM are calculated with respect to the full-order thermal model at each heat transfer time step using Eqs. (30) and (31). In the case of the thermal ROM, the vectors "Full" and "ROM" correspond to the temperatures vectors from the full-order and reduced-order thermal models at a given time step. To eliminate any additional errors, the full-order structural model is used for both cases. Time-histories of the NRMSE and L_∞ error for a simulation time of 1,200 s are given in Fig. 26(a) and Fig. 26(b), respectively. Examining these figures, the thermal ROM shows good agreement with the full-order thermal model.

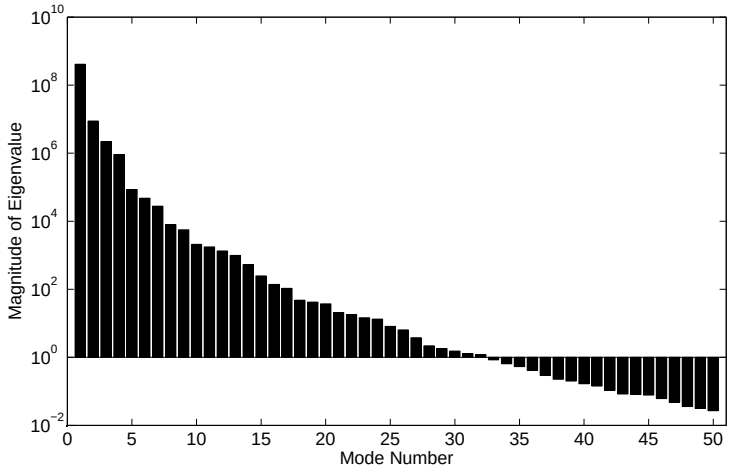

Figure 25. Eigenvalues associated with first 50 thermal POD modes based on 49,510 thermal snapshots.

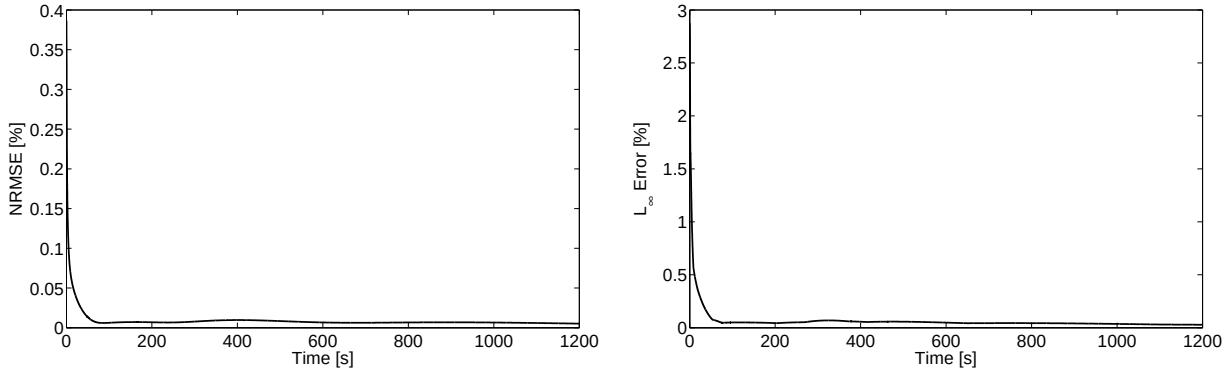

(a) NRMSE. (b) L_∞ error.

Figure 26. NRMSE and L_∞ error of thermal POD ROM at $M_\infty = 6.5$, $\alpha = 2^\circ$, and $h = 35$ km.

The next step is to obtain the upper and lower bounds for each of the 32 POD modal coordinates using the procedure described above. The maximization/minimization procedures are performed using the function `fmincon` available within Matlab®. Note that the minimization/maximization steps are repeated at different starting locations within the parameter space in order to avoid the potential for obtaining local extrema. Plots of the upper and lower bounds of each of the 32 POD modal coordinates are given in Fig. 27(a) and Fig. 27(b), respectively.

In order to verify that the bounds identified in Fig. 27 are indeed the maximum upper bounds and minimum lower bounds over the range of flight conditions given in Table 3, an additional set of ten aerothermoelastic simulations is run. The Mach number, angle of attack, and altitude for these simulations are selected by using the LHS methodology along with the criterion to maximize the minimum Euclidean distance between the flight conditions of the ten new simulations and the ten simulations that were used in establishing the bounds originally. The additional ten simulations make use of the thermal ROM that consists of the 32 retained POD modes, however, the full-order structural model is used to calculate the structural dynamic response. The time step sizes for the additional simulations are the same as those that were used

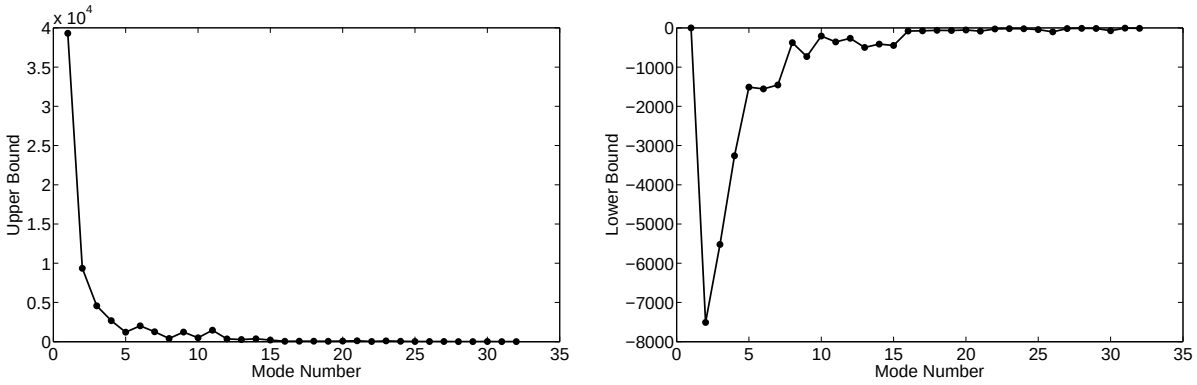

(a) Upper bounds.

(b) Lower bounds.

Figure 27. Upper and lower bounds of POD modal coordinates for 32 retained POD basis vectors.

in the original ten aerothermoelastic simulations. At each heat transfer time step, the vector of POD modal coordinates is stored. The maximum and minimum value of each POD modal coordinate over all time steps over all of the ten simulations is then found. The bounds identified using the procedure shown in Fig. 24 are compared with the minimum/maximum values identified via the ten additional aerothermoelastic simulations by computing margins of safety. The margin of safety for the upper bounds, MS_U, and margin of safety for the lower bounds, MS_L, are found using

$$\mathrm{MS}_{U,i} = \frac{\mathrm{ub}_i - \max_i}{|\max_i|} \times 100\% \tag{46a}$$

$$\mathrm{MS}_{L,i} = -\frac{\mathrm{lb}_i - \min_i}{|\min_i|} \times 100\%, \tag{46b}$$

where ub_i and lb_i are the upper and lower bounds for the i-th POD modal coordinate, and $\max_i$ and $\min_i$ are the maximum and minimum values of the i-th modal coordinate identified from the ten additional aerothermoelastic simulations. In order for the upper and lower bounds to encompass the ranges of the POD modal coordinates experienced in the simulations, all elements of both MS_U and MS_L must be greater than or equal to zero. Plots of MS_U and MS_L are given in Fig. 28(a) and Fig. 28(b), respectively. In both figures, all values of MS are greater than or equal zero, and thus the bounds are valid. Note that the data point corresponding to mode 1 in Fig. 28(b) is not shown because both $\min_1$ and lb_1 are zero.

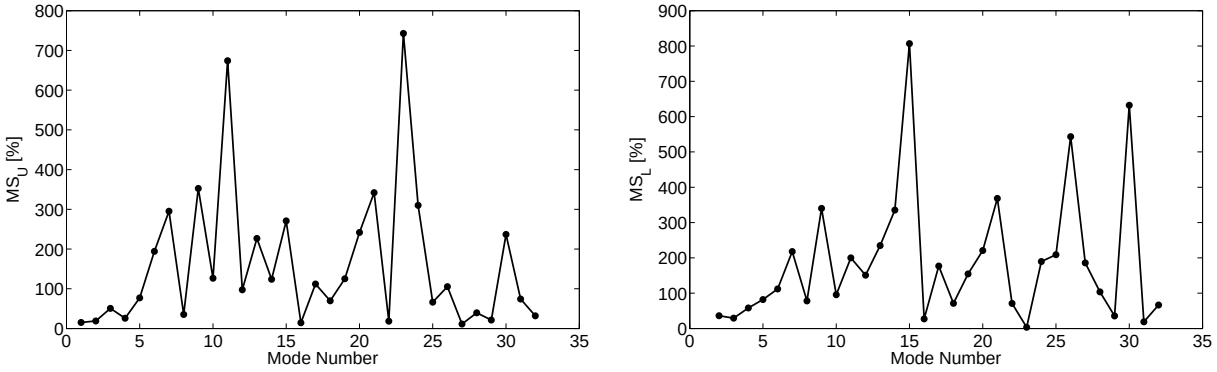

(a) Margins of safety on upper bounds.

(b) Margins of safety on lower bounds.

Figure 28. Margins of safety on upper and lower bounds based on ten additional aerothermoelastic simulations.

Due to the prohibitive computational expense, it is not feasible to use all 32 POD modal coordinates as design variables in the kriging representations of the stiffness matrix and thermal load vector. While all 32 POD modes will be used in the solution of the reduced thermal system, only a subset of the resulting POD modal coordinates will be passed to the kriging functions at each aeroelastic time step. Though some

accuracy will be lost in representing the physical temperatures using less than 32 POD modes, the penalty is not expected to be significant due to the fact that the POD modes are sorted in order of decreasing energy and the modes that are excluded from the kriging models are chosen to be the lowest energy modes.

The number of number of design variables, number of sample points, and order of regression must be selected for both the kriging model of the thermal loads and the kriging model of the generalized stiffness. In selecting these parameters, consideration must be given to a variety of factors. The number of sample points used to generate the kriging ROMs must be sufficient to provide enough training information to achieve the desired level of accuracy. Additionally, if too few design variables are used, the temperature distribution passed to the kriging model may not be representative of the actual temperature distribution. Finally, the computation time required to generate the kriging ROMs must be balanced against the desired accuracy, number of sample points, and number of design variables required to obtain this accuracy for a given regression model. Because the computation time increases quickly with number of sample points, number of design variables, and order of regression, the trade-off between desired accuracy and computation time must be taken into account. Though the kriging models are generated *a priori* and off-line, the computation time required to generate them must still be on a reasonable order.

A summary of the parameters selected for the two kriging models as well as the errors over 500 evaluation cases are given in Table 4. The last three columns in the table give the CPU times required to generate the kriging training data, t_T, create the kriging ROMs, t_K, and evaluate the kriging ROMs, t_E. Though the two ROMs use a different number of sample points to generate the models, both use 500 evaluation points for determining the accuracy of the ROMs. Note that t_E is greating for the kriging model of $k_S^*(T)$ than for that of $F_S^H(T)$ due to the longer computation required to compute $k_S^*(T)$ at each evaluation point. For the kriging model of the generalized stiffness, 20 design variables, 500 sample points and a 2nd order regression model are used. For the resulting kriging model based on the ten free vibration modes employed above, the average NRMSE and maximum L_∞ error over 500 evaluation points are found to be 0.05% and 1.3%, respectively. Because the generalized stiffness matrix is dependent on the structural basis, this kriging ROM must be updated each time the basis is changed. However, because less sample points and a lower order regression model are required, the computational cost of generating the kriging ROM of the generalized stiffness matrix is less than that required to generate the kriging ROM of the thermal load vector. For the kriging model of the thermal loads, 20 design variables, 5,000 sample points and a 3rd order regression model are used. For the resulting kriging model, the average NRMSE and maximum L_∞ error over 500 evaluation points are found to be 0.1% and 4.7%, respectively. Because kriging is used to represent the physical thermal load vector as opposed to the generalized one, this model is independent of the structural basis and does not need to be updated if the structural basis changes. Therefore, this kriging model of the thermal loads is used for the remainder of this paper. As both kriging models use 20 design variables, the first 19 design variables are the POD modal coordinates of the corresponding POD modes, and the 20th design variable represents the uniform initial condition as described previously.

Table 4. Parameters for kriging ROMs of $k_S^*(T)$ and $F_S^H(T)$.

Model	n_{dv}	n_k	$\mathcal{O}$	Avg NRMSE [%]	Max L_∞ [%]	t_T [hrs][a]	t_K [hrs][a]	t_E [hrs][a]
$k_S^*(T)$	20	500	2nd Order	0.051	1.33	0.81	0.051	0.78
$F_S^H(T)$	20	5,000	3rd Order	0.12	4.68	5.61	71	0.55

[a] 1 2.53-GHz Intel Xeon E5540 processor, 3.0 GB RAM.

As the motivation for the use of the kriging ROMs is to improve the computational cost of the structural dynamic solution, the computational savings achieved via the use of these ROMs must be quantified. To do so, the full-order and reduced-order structural solutions are each run for 10 time steps. The full-order solution consists of calling Nastran to generate the equations of motion in physical space and marching the solution forward one time step. The reduced-order solution consists of using the kriging ROMs to generate the equations of motion in modal space and marching the solution forward one time step. For both the full-order and reduced-order solutions, the computation time is recorded for each of the ten time steps. The maximum and minimum computation times are removed for each case, and the the remaining eight values are averaged to determine the average computation time for the reduced-order and full-order models. The average computation time for the full-order structural model was found to be 7.22 s while that for the

reduced-order structural model was found to be 1.42 s, resulting in an improvement in computational cost by a factor of 5. Note that in both the full-order and reduced-order cases, the simulations were performed using one 2.53-GHz Intel Xeon E5540 processor with 3.0 GB RAM.

VIII. Techniques for Enhanced Modal Solutions

Recall that the generalized quantities in section VII.B were calculated based on the first ten structural free vibration modes. Because the focus of that section was on the accuracy of the kriging ROMs, the ability of the chosen structural modes to represent the structural dynamic response within an aerothermoelastic environment was not examined. Previous work[14] has shown that the use of free vibration modes alone within a mode-displacement approach may not always be sufficient to capture the structural dynamic response under the aerodynamic and thermal loads experienced in hypersonic flight. Thus, the goal of the current section is to examine techniques for improving the modal representation of the structural dynamic response while still maintaining the low-order nature of the solution. Because both the thermal and structural ROMs consist of modal solutions, the techniques discussed are applicable to both. However, in this paper the techniques are applied only to the structural dynamic model. The following sections discuss a technique for obtaining robust and accurate modal solutions for the structural dynamic response of hypersonic vehicle structures.

VIII.A. Load-Dependent Ritz Vector Formulation

The technique used in this study to improve the accuracy of the structural ROM involves augmentation of the original basis with additional Ritz vectors. The methodology is intentionally general so that it can be applied to both the structural dynamic and thermal response problems, but it is employed specifically for the structural dynamic response problem in this paper. In this approach, the original structural basis containing the reference free vibration modes is augmented by inserting additional columns into the modal matrix, i.e.,

$$\Phi_S = \left[\begin{array}{cccc|ccc} \phi_1^{(1)} & \phi_1^{(2)} & \cdots & \phi_1^{(r)} & \psi_1^{(1)} & \cdots & \psi_1^{(l)} \\ \phi_2^{(1)} & \phi_2^{(2)} & \cdots & \phi_2^{(r)} & \psi_2^{(1)} & \cdots & \psi_2^{(l)} \\ \vdots & \vdots & \ddots & \vdots & \vdots & \ddots & \vdots \\ \phi_s^{(1)} & \phi_s^{(2)} & \cdots & \phi_s^{(r)} & \psi_s^{(1)} & \cdots & \psi_s^{(l)} \end{array}\right], \tag{47}$$

where $\psi^{(i)}$ represents the i-th augmented mode shape and l is the number of augmented modes. The specific technique used in this work to obtain the augmented mode shapes is the method of load-dependent Ritz vectors.[39] This approach is advantageous in that it allows for the ability to capture quasi-static response due to slowly changing loads. Additionally, it provides the capability for capturing structural response that might otherwise not be contained within a particular eigenvector subspace. This is because even if the frequency of a particular eigenmode is contained in the frequency of the loading, if the spatial distribution of the loading is orthogonal to that of the eigenvector, that specific eigenvector will not contribute to the solution. Thus, load-dependent Ritz vectors provide a means for incorporating the spatial distribution of the loads into the modal representation of the structural dynamics. Load-dependent Ritz vectors can be used to augment the original basis, whether it is obtained from an eigenvalue solution in the case of the structural ROM, or from POD in the case of the thermal ROM.

A summary of the algorithm for computing load-dependent Ritz vectors is given in Table 5. The procedure begins by selecting a set of free vibration modes, ϕ. In this application the number of free vibration modes, r, is determined based on a cut-off frequency beyond which the corresponding mode shapes are not expected to contribute to the solution. The physical mass matrix, M_S, and modified stiffness matrix at a reference thermal state, K_S^*, are then obtained from the finite element model and K_S^* is decomposed into its LU factorization for efficient inversion. The first load-dependent Ritz vector, $\bar{\psi}^{(1)}$, is computed in step 4 by solving the static problem given by

$$K_S^* \bar{\psi}^{(1)} = F_S^I, \tag{48}$$

where F_S^I is a user-determined input. The quality of the load-dependent Ritz vectors is dependent on the degree to which F_S^I represents the loading that the structure will experience in the actual simulation. In order to make $\bar{\psi}^{(1)}$ orthogonal to the previously determined free vibration modes with respect to M_S, the modified Gram-Schmidt algorithm is invoked in step 5 which repeatedly removes from $\bar{\psi}^{(1)}$ its projection

onto the previous modes according to

$$\bar{\psi}^{(1)} = \bar{\psi}^{(1)} - \phi^{(j)}\phi^{(j)T}M_S\bar{\psi}^{(1)}, \quad j = 1, \ldots, r. \tag{49}$$

In Eq. (49), each time $\bar{\psi}^{(1)}$ is updated it overwrites the previous version, thus reducing storage requirements. Note that the modified Gram-Schmidt algorithm is used in order to avoid the well-known numerical instabilities associated with the classical Gram-Schmidt algorithm. The orthogonalized solution vector $\bar{\psi}^{(1)}$ is then normalized with respect to the mass matrix to obtain $\psi^{(1)}$ using

$$\psi^{(1)} = \frac{\bar{\psi}^{(1)}}{\left(\bar{\psi}^{(1)T}M_S\bar{\psi}^{(1)}\right)^{1/2}}. \tag{50}$$

The static solution used to obtain $\psi^{(1)}$ neglected the inertial forces which are given by $M_S\ddot{\psi}^{(1)}$. Assuming harmonic motion in free vibration, the neglected inertial forces are of the form $\omega^2 M_S\psi^{(1)}$, where ω represents a typical frequency of the load. The vector of neglected inertial loads is then applied as a load vector in the generation of $\bar{\psi}^{(2)}$ at step 8. Again, a static solution is used to obtain $\bar{\psi}^{(2)}$, and $\psi^{(2)}$ is obtaining by orthogonalizing in mass against all other modes and normalizing with respect to the mass matrix. Steps 8 – 11 are repeated until the desired number of load-dependent Ritz vectors are obtained. The procedure depicted in Table 5 shows the steps taken when a single load vector, F_S^I, is specified. The algorithm can be generalized for the case in which multiple different load vectors are specified. In this case, steps 4 – 11 are repeated for each F_S^I and each time a new load-dependent Ritz vector, $\bar{\psi}$, is calculated, it is orthogonalized against all previous vectors with respect to M_S, and normalized with respect to M_S. This study will investigate the effect of number of specified load vectors, n_F, and number of load-dependent Ritz vectors per specified load vector, n_R, on solution accuracy. Note that n_R corresponds to the number of iterations performed in steps 7 – 11.

Table 5. Algorithm for generation of load-dependent Ritz vectors.[39]

1.	Select r free vibration modes, ϕ	
2.	Obtain M_S and K_S^*	
3.	$K_S^* = LU$	Decompose K_S^* for efficient inversion
4.	$K_S^*\bar{\psi}^{(1)} = F_S^I$	Specify F_S^I and solve for $\bar{\psi}^{(1)}$
5.	for $j = 1, \ldots, r$	Orthogonalize $\bar{\psi}^{(1)}$ against free vibration modes w.r.t. M_S
	$\bar{\psi}^{(1)} = \bar{\psi}^{(1)} - \phi^{(j)}\phi^{(j)T}M_s\bar{\psi}^{(1)}$	Modified Gram-Schmidt algorithm
	end	
6.	$\psi^{(1)} = \frac{\bar{\psi}^{(1)}}{\left(\bar{\psi}^{(1)T}M_S\bar{\psi}^{(1)}\right)^{1/2}}$	Normalize $\bar{\psi}^{(1)}$ w.r.t. M_S
7.	for $i = 2, \ldots, l$	Loop to generate subsequent vectors
8.	$K_S^*\bar{\psi}^{(i)} = M_S\psi^{(i-1)}$	Solve for $\bar{\psi}^{(i)}$ based on neglected inertia
9.	for $j = 1, \ldots, r$	Orthogonalize $\bar{\psi}^{(i)}$ against free vibration modes w.r.t. M_S
	$\bar{\psi}^{(i)} = \bar{\psi}^{(i)} - \phi^{(j)}\phi^{(j)T}M_s\bar{\psi}^{(i)}$	Modified Gram-Schmidt algorithm
	end	
10.	for $j = 1, \ldots, i-1$	Orthogonalize $\bar{\psi}^{(i)}$ against Ritz modes w.r.t. M_S
	$\bar{\psi}^{(i)} = \bar{\psi}^{(i)} - \psi^{(j)}\psi^{(j)T}M_s\bar{\psi}^{(i)}$	Modified Gram-Schmidt algorithm
	end	
11.	$\psi^{(i)} = \frac{\bar{\psi}^{(i)}}{\left(\bar{\psi}^{(i)T}M_S\bar{\psi}^{(i)}\right)^{1/2}}$	Normalize $\bar{\psi}^{(i)}$ w.r.t. M_S
12.	end	Assemble modal matrix, Φ_S

The main challenge associated with this approach is determining the representative load vectors, F_S^I, to use in step 4 of Table 5. As the quality of the basis is dependent on the choice of F_S^I, it is important to choose these vectors so that they most closely represent the spatial distribution of loads that the structure will experience during flight. In order to identify the dominant spatial components of the loads, a POD analysis is applied to the structural load vector, F_S, based on snapshots of F_S from high-fidelity aerothermoelastic

simulations. As discussed in section II, the POD is optimal in the sense that it arranges the modes such that the first mode contains the largest amount of energy, the second mode contains the second largest amount of energy, and so on. As a result of this optimality property of the proper orthogonal modes, POD can be used to identify the most dominant spatial components of the structural loads for use in the load-dependent Ritz vector procedure. The algorithm shown in Table 5 will be repeated for a specified number of representative load vectors resulting in a set of load-dependent Ritz vectors to be appended to the set of free vibration modes.

As in the case of the POD procedure for the thermal ROM, snapshots of the structural load vector, F_S, must be collected to derive the corresponding POD basis vectors. These snapshots of the structural load include contributions due to both thermal loads and aerodynamic loads, i.e.,

$$F_S(t) = F_S^H(t) + F_S^A(t) \tag{51}$$

The snapshots are taken by running an aerothermoelastic simulation for a period of 3,000 s. This simulation uses the thermal ROM with the 32 previously identified thermal POD modes. For the structural dynamic solution, the full-order model is used. The flight conditions for this simulation are: $M_\infty = 6.5$, $\alpha = 2^\circ$, $h = 35$ km, corresponding to the mid-points of the ranges given in Table 3. The initial temperature distribution is taken to be uniform 293 K. The time steps for the various solution components are as follows: $\Delta t_{AE} = \Delta t_{HT} = 0.1$ s, $\Delta t_{AT} = 1$ s. The structural load vector is stored at the end of each aerothermal time step resulting in a total of 3,000 snapshots. Once the snapshots are obtained, the snapshot matrix is assembled by storing each snapshot as a column in the snapshot matrix. The POD basis is then calculated by taking the singular value decomposition of the snapshot matrix. The eigenvalues corresponding to the first 50 POD modes are given Fig. 29. In the next section, the effect of number of POD modes of F_S and number of load-dependent Ritz vectors per POD mode on solution accuracy are examined.

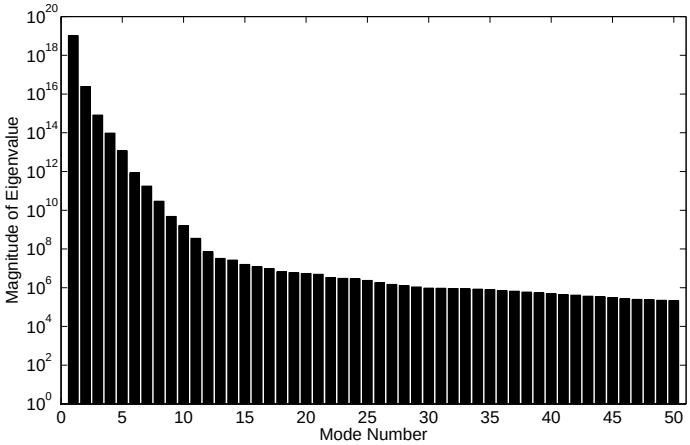

Figure 29. Eigenvalues associated with first 50 POD modes of F_S based on 3,000 snapshots.

VIII.B. Load-Dependent Ritz Vector Results: Case 1

To exercise the load-dependent Ritz vector formulation described above, aerothermoelastic simulations of the control surface model are carried out using both the full-order and reduced-order structural dynamic models. The full-order model is treated as the truth model and its solution is obtained by solving the equations of motion in physical space given by Eq. (6). For the full-order model, the equations of motion are generated directly using Nastran. Recall that the full-order and reduced-order models are both solved using the same Newmark-β integration scheme described in section III to eliminate discrepancies due to different numerical integration methods. The reduced-order model consists of the solving the modal equations of motion given in Eq. (9) where the structural modal matrix, Φ_S, can contain both reference free vibration modes and load-dependent Ritz vectors obtained using the formulation outlined in the previous section. The reduced-order model can update the equations of motion at each aeroelastic time step by calling Nastran directly or by using the kriging ROMs of the generalized stiffness matrix and physical thermal load vector obtained using the parameters n_{dv}, n_k, and $\mathcal{O}$ in Table 4. Both the full-order model and reduced-order model make use of

the thermal ROM with the 32-mode basis obtained in section VII.B.1. For the structural ROM, the basis consists of a pre-determined set of free vibration modes appended with a set of load-dependent Ritz vectors. For all studies in the current section, the number of free vibration modes, n_V, is taken to be six and the mode shapes are chosen to be the first six of the ten reference modes employed in section VII.B based on a cut-off frequency of 100 Hz. This six-mode subset has a maximum frequency of 94.9 Hz. The goal of this section is to assess the effect of number of specified load vectors, n_F, and number of load-dependent Ritz vectors per specified load vector, n_R, on the accuracy of the reduced-order structural dynamic model. Note that the total number of structural basis vectors is equal to $n_V + (n_F)(n_R)$.

To quantify the error between the full-order and reduced-order structural dynamic models, the NRMSE and L_∞ error metrics, given in Eqs. (30) and (31), are employed. In this case, the quantities "Full" and "ROM" are taken to be vectors of z-direction displacements for nodes at the OML from the full-order and reduced-order models, respectively. The parameters for the aerothermoelastic simulations used in this part of the study are given in Table 6. The total simulation time for this case is chosen to be 600 s.

Table 6. Parameters used for load-dependent Ritz vector case 1.

Case	M_∞	α	h [km]	Δt_{AE} [s]	Δt_{HT} [s]	Δt_{AT} [s]	T_0 [K]
1	8	4°	35	0.1	0.1	1	293

Before assessing the effect of load-dependent Ritz vectors, the impact of using kriging ROMs to generate $k_S^*(T)$ and $F_S^H(T)$ on the accuracy of the solution must first be addressed. Doing so provides insight into how much of the solution error can be attributed to error associated with the kriging ROMs as opposed to error associated with the reduced structural basis. To accomplish this, aerothermoelastic simulations are carried out for the flight conditions of case 1 for three different subcases that are summarized in Table 7. For the subcase 1a, the full-order structural model is used in the simulation and the results are treated as the truth model. Subcase 1b consists of using the structural ROM with the only the six free vibration modes, (i.e., $n_V = 6$ $n_F = 0$, $n_R = 0$), and using Nastran to compute $k_S^*(T)$ and $F_S^H(T)$ at each aeroelastic time step. Subcase 1c consists of using the structural ROM again with the six free vibration modes, but employing the kriging ROMs to compute $k_S^*(T)$ and $F_S^H(T)$. It is expected that the 6-mode basis will not adequately capture the structural response represented by the full-order model. However, the goal of subcases 1a - 1c is not to assess the error associated with the reduced structural basis, but rather to evaluate the error incurred by employing the kriging models to approximate $k_S^*(T)$ and $F_S^H(T)$.

Table 7. Parameters for aerothermoelastic subcases used to assess error incurred due to kriging ROMs of $k_S^*(T)$ and $F_S^H(T)$.

Subcase	Structural Model	n_V	n_F	n_R	Method for Computing $k_S^*(T)$, $F_S^H(T)$
1a	Full-order	N/A	N/A	N/A	N/A
1b	ROM	6	0	0	Nastran
1c	ROM	6	0	0	Kriging ROMs

To assess the response levels, the z-direction displacements of node 247 (located at the mid-chord of the tip on the bottom surface) are plotted for each of the three subcases given in Table 7. Results are given in Fig. 30. To quantify the error incurred due solely to the kriging ROMs of $k_S^*(T)$ and $F_S^H(T)$, the NRMSE and L_∞ error metrics are computed for subcase 1c with respect to subcase 1b. Plots of the NRMSE and L_∞ over time are given in Fig. 31(a) and Fig. 31(b), respectively. The error metrics show an initial high error which is due to the fact that the simulation begins with the structure in the undeformed configuration. Therefore, the structural displacements are small in the initial part of the transient, which results in a small denominator in Eqs. (30) and (31), and therefore a large value of error early in the transient. However, within 10 seconds into the transient, the NRMSE and L_∞ error decrease to below 10% and 20%, respectively, and remain below these values for the remainder of the simulation.

With the error due to the kriging ROMs of $k_S^*(T)$ and $F_S^H(T)$ quantified, the next step is to assess the effect of inclusion of load-dependent Ritz vectors on the accuracy of the structural ROM. For all cases from this point forward, the kriging ROMs of $k_S^*(T)$ and $F_S^H(T)$ are used within the structural ROM. The goal of this aspect of the study is to assess the solution accuracy as a function of n_F and n_R. A summary of the

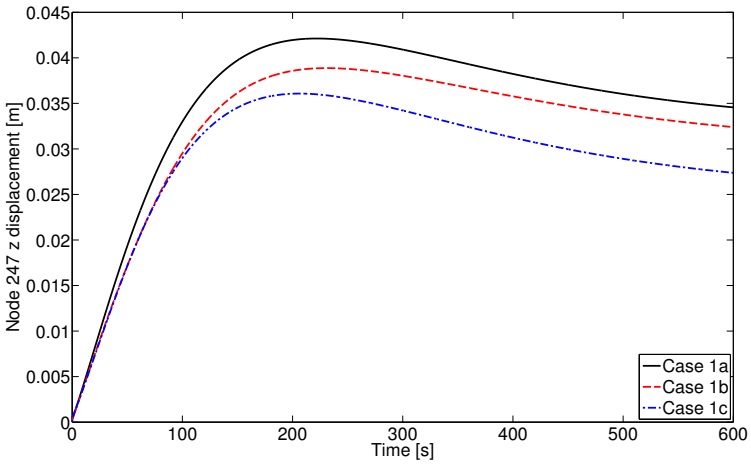

Figure 30. Node 247 z displacements for subcases 1a, 1b, and 1c.

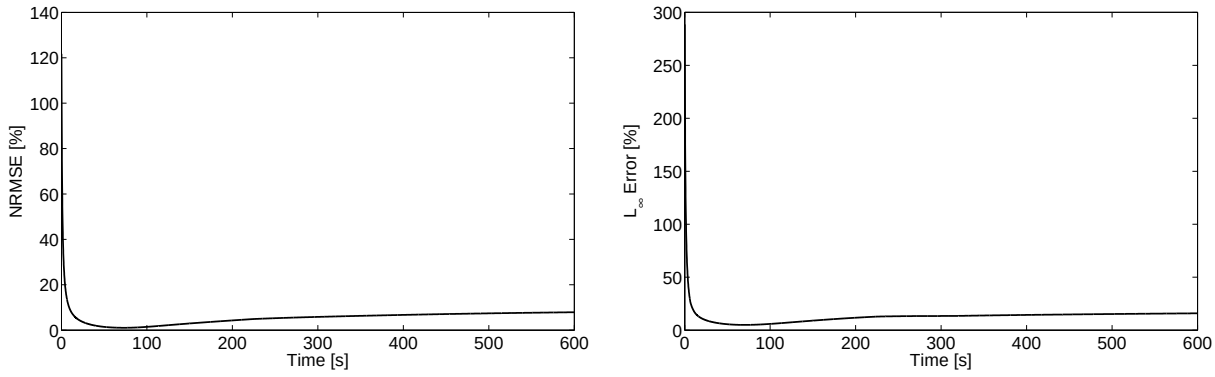

(a) NRMSE. (b) L_∞ error.

Figure 31. Error of subcase 1c with respect to subcase 1b illustrating error incurred due kriging ROMs of $k_S^*(T)$ and $F_S^H(T)$.

subcases used to perform this assessment is given in Table 8. Note that the errors for these subcases are computed with respect to subcase 1a in Table 7 and therefore they include both error due to the kriging ROMs as well as error due to structural basis truncation.

Table 8. Parameters for aerothermoelastic subcases used to assess effect of load-dependent Ritz vectors on structural ROM.

Subcase	Structural Model	n_V	n_F	n_R	Method for Computing $k_S^*(T)$, $F_S^H(T)$
1c	ROM	6	0	0	Kriging ROMs
1d	ROM	6	1	1	Kriging ROMs
1e	ROM	6	10	1	Kriging ROMs
1f	ROM	6	1	10	Kriging ROMs

Plots of the NRMSE and L_∞ errors of subcases 1c - 1f with respect to subcase 1a are given in Fig. 32(a) and Fig. 32(b), respectively. Examining these figures, it is observed that the inclusion of load-dependent Ritz vectors in addition to the six free vibration modes results in a noticeable improvement in the structural ROM. It should be noted that there is inherent error in the structural ROM due to the use of the kriging ROMs to approximate $k_S^*(T)$ and $F_S^H(T)$, and thus the overall error of the structural ROM cannot be reduced to zero. Comparing Fig. 32 to Fig. 31, it can be observed that the error due to basis truncation has been reduced and the errors shown in Fig. 32 approach or surpass those shown in Fig. 31, especially for subcases 1e and 1f. Comparing subcase 1d to subcases 1e and 1f, it is observed that the inclusion of only one load-dependent Ritz vector in the basis does not provide the level of accuracy obtained by including multiple load-dependent Ritz vectors. The greatest difference in L_∞ error beyond 10 s between subcases 1e and 1f occurs at 78.1 s with the L_∞ error of subcase 1e being 11.2% lower than that of subcase 1f. This is not surprising as the structural response is dominated by the slowly changing thermal loads for this case, and therefore inertial effects are not significant. The maximum improvement in L_∞ error of subcase 1e with respect to subcase 1c beyond 10 s is 45% and occurs at 590.1 s. Subcase 1e gives an average improvement in L_∞ error of 38% over subcase 1c, demonstrating the advantage of using load-dependent Ritz vectors.

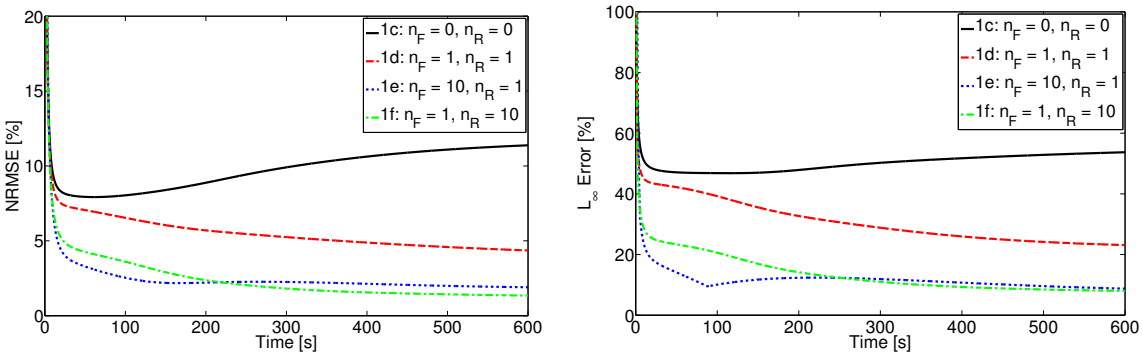

(a) NRMSE. (b) L_∞ error.

Figure 32. Total error of structural ROMs (subcases 1c - 1f) with respect to full-order structural model (subcase 1a) using different structural bases.

VIII.C. Load-Dependent Ritz Vector Results: Case 2

Because the above case displays a low level of unsteadiness in the structural dynamic response, load-dependent Ritz vectors corresponding to static solutions were found to provide a significant benefit in improving the accuracy of the structural ROM. However, consideration of inertial effects when computing the basis may be necessary for cases which exhibit a higher level of unsteadiness in the structural dynamic response. The extent to which load-dependent Ritz vectors impact the structural dynamic solution is now examined for such a case. To excite higher levels of unsteadiness in the structure, time-dependent motion is prescribed at the attachment point as opposed to imposing fixed boundary conditions. The goal of applying

this excitation is to mimic the motion at the fuselage-control surface interface that would occur in a full vehicle configuration as a result of vehicle rigid body motion and fuselage structural dynamic response.

For a structure with prescribed accelerations and displacements at degrees-of-freedom (DOFs) r, the equations of motion can be partitioned as

$$\begin{bmatrix} M_{rr} & M_{ru} \\ M_{ur} & M_{uu} \end{bmatrix} \begin{Bmatrix} \ddot{x}_r \\ \ddot{x}_u \end{Bmatrix} + \begin{bmatrix} K^*_{rr} & K^*_{ru} \\ K^*_{ur} & K^*_{uu} \end{bmatrix} \begin{Bmatrix} x_r \\ x_u \end{Bmatrix} = \begin{Bmatrix} F^H_r + F^A_r + F^{BC}_r \\ F^H_u + F^A_u \end{Bmatrix}, \tag{52}$$

where the subscript r corresponds to the restrained DOFs (those with prescribed accelerations and displacements), the subscript u corresponds to the unrestrained DOFs (those without prescribed accelerations and displacements), and F^{BC}_r represents the reaction force exerted by the fuselage (body) on the control surface required to obtain this motion. Note that the subscript S is removed from the matrix and vector quantities in this section and all equations are assumed to be associated with the structural dynamics system as opposed to the thermal system. In this formulation, the equations of motion for the unrestrained DOFs are cast in terms of the elastic displacements relative to the rigid body motion caused by the enforced displacements at the restrained DOFs. The first step is to calculate the rigid body displacements due to enforced motion at the unrestrained DOFs, denoted by x^R_u. This quantity is obtained by neglecting inertial loads and external loads in the second row of Eq. (52) and solving for x_u, i.e.

$$x^R_u = -(K^*_{uu})^{-1} K^*_{ur} x_r. \tag{53}$$

Note that a transformation, U, can be defined in Eq. (53) between x^R_u and x_r such that

$$x^R_u = U x_r \text{ , where } U = -(K^*_{uu})^{-1} K^*_{ur}. \tag{54}$$

If the number of DOFs with prescribed motion were exactly equal to the minimum number of DOFs required to constrain rigid body motion, the columns of U would represent rigid body modes. Because in this case the number of DOFs with prescribed motion is greater than that required to constrain rigid body motion, the columns of U represent constraint modes.

The next step is to derive the equations governing the elastic deformation of the unrestrained DOFs, x^E_u, relative to the rigid body displacement. Expanding Eq. (52), one obtains

$$M_{rr}\ddot{x}_r + M_{ru}\ddot{x}_u + K^*_{rr}x_r + K^*_{ru}x_u = F^H_r + F^A_r + F^{BC}_r \tag{55a}$$

$$M_{ur}\ddot{x}_r + M_{uu}\ddot{x}_u + K^*_{ur}x_r + K^*_{uu}x_u = F^H_u + F^A_u. \tag{55b}$$

Recall that the total motion of the unrestrained DOFs is the sum of the rigid body motion plus the elastic motion, i.e.,

$$x_u = x^R_u + x^E_u. \tag{56}$$

Substituting Eq. (56) into Eq. (55b), one obtains

$$M_{ur}\ddot{x}_r + M_{uu}\left(\ddot{x}^R_u + \ddot{x}^E_u\right) + K^*_{ur}x_r + K^*_{uu}\left(x^R_u + x^E_u\right) = F^H_u + F^A_u, \tag{57}$$

and using Eq. (53) in Eq. (57), the system becomes

$$M_{ur}\ddot{x}_r + M_{uu}\left[-(K^*_{uu})^{-1}K^*_{ur}\ddot{x}_r + \ddot{x}^E_u\right] + K^*_{ur}x_r + K^*_{uu}\left[-(K^*_{uu})^{-1}K^*_{ur}x_r + x^E_u\right] = F^H_u + F^A_u. \tag{58}$$

Bringing all terms associated with the restrained DOFs to the right-hand side of Eq. (58), the equation becomes

$$M_{uu}\ddot{x}^E_u + K^*_{uu}x^E_u = -M_{ur}\ddot{x}_r + M_{uu}(K^*_{uu})^{-1}K^*_{ur}\ddot{x}_r - K^*_{ur}x_r + K^*_{uu}(K^*_{uu})^{-1}K^*_{ur}x_r + F^H_u + F^A_u, \tag{59}$$

and simplifying the right-hand side of Eq. (59) results in

$$M_{uu}\ddot{x}^E_u + K^*_{uu}x^E_u = \left[M_{uu}(K^*_{uu})^{-1}K^*_{ur} - M_{ur}\right]\ddot{x}_r + F^H_u + F^A_u. \tag{60}$$

The relation given by Eq. (60) is the system to be solved for the relative elastic motion of the unrestrained DOFs, x^E_u. Because the system has been cast in terms of the elastic displacements relative to the rigid body motion, the modal matrix does not need to be modified to include rigid body modes or constraint modes.

Note that the solution to Eq. (60) requires only the accelerations of the restrained DOFs, $\ddot{x}_r$, and not the displacements. However, the displacements of the restrained DOFs are required in order to compute the rigid body motion using Eq. (53). As before, the reduced-order system is obtained by first representing the elastic motion, $x_u^E(t)$, as a linear combination of the reference free vibration modes such that

$$x_u^E(t) = \Phi_S d(t), \tag{61}$$

where d represents the modal coordinates of the reference modes which are stored as columns of the modal matrix, Φ_S. Again, the system is reduced by substituting Eq. (61) into Eq. (60) and pre-multiplying the system by Φ_S^T to project the system onto the basis, i.e.

$$\Phi_S^T M_{uu} \Phi_S \ddot{d}(t) + \Phi_S^T K_{uu}^*(T) \Phi_S d(t) = \Phi_S^T F_u(t), \tag{62}$$

where the net force, F_u, is given by

$$F_u = \left[M_{uu} (K_{uu}^*)^{-1} K_{ur}^* - M_{ur} \right] \ddot{x}_r(t) + F_u^H(t) + F_u^A(t). \tag{63}$$

The temperature-dependent generalized stiffness matrix, given by $\Phi_S^T K_{uu}^*(T) \Phi_s$ in Eq. (62), is updated at every time step using the previously described kriging model. However, the stiffness matrix partitions K_{uu}^* and K_{ur}^* in Eq. (63) are evaluated at the reference thermal state and held constant throughout the simulation due to the computational cost associated with updating these matrices.

The motion of the attachment point is modeled using the relation

$$w_a(t) = \eta \sin(\omega t), \tag{64}$$

where w_a refers to the displacement of the z-direction degrees of freedom at the attachment point, η is a real scaling coefficient, and ω is a frequency that corresponds to a fuselage natural frequency. For this case, η is taken to be 0.06 and ω is chosen to be 43.3 rad/s (6.9 Hz) which is the natural frequency of the fuselage second bending mode based on the vehicle structural parameters given in a recent work.[40] The flight conditions and time step sizes used for this case are given in Table 9. The aeroelastic time step size is determined based on the desire to resolve the highest frequency free vibration mode with a minimum of 10 temporal sampling points within one cycle. Of the six free vibration modes at the reference thermal state, the highest frequency is 94.9 Hz, and thus Δt_{AE} is chosen to be 0.001 s to account for the fact that the actual frequency may be slightly higher at lower temperatures. The initial temperature condition, denoted "400 s cruise" in the table, is obtained by marching the aerothermal solution forward in time for 400 s. The temperature distribution obtained at the end of this period is stored and used as the initial temperature distribution for the full aerothermoelastic simulation. This approach for obtaining the initial temperatures is used so that the structure will begin from a thermally deformed state and the structural dynamic response will include both the effect of slowly changing thermal loads as well as that of the base excitation. For this case, the thermal loads are held constant and the aerodynamic pressure loads are set to zero.

Table 9. Parameters for load-dependent Ritz vector case 2.

Case	M_∞	α	h [km]	Δt_{AE} [s]	T_0 [K]
2	6.5	2°	35	0.001	400 s cruise

To assess the ROM accuracy, the z-direction displacements are obtained from the full-order model as well as the ROM using different basis sets. The three subcases which are simulated are given in Table 10. Results are plotted for the mid-chord, mid-span location on the bottom surface (node 238) and the mid-chord, tip location on the bottom surface (node 247) in Fig. 33(a) and Fig. 33(b), respectively. Examining the figures, it is observed that the ROM displays some difficulty in capturing the response at the tip. Furthermore, there is not a significant improvement in ROM accuracy by including load-dependent Ritz vectors for this particular case. In addition to the results shown, alternative basis sets were tried which contained load-dependent Ritz vectors based on the base excitation loads, but a significant improvement in the ROM was still not observed. Therefore, further investigation into improving the ROM error under base excitation is warranted. However, such studies are reserved for future work.

Table 10. Parameters for aerothermoelastic simulations used to assess ROM accuracy under base excitation.

Subcase	Structural Model	n_V	n_F	n_R	Method for Computing $k_S^*(T)$, $F_S^H(T)$
2a	Full-order	N/A	N/A	N/A	N/A
2b	ROM	6	0	0	Kriging ROMs
2c	ROM	6	1	10	Kriging ROMs

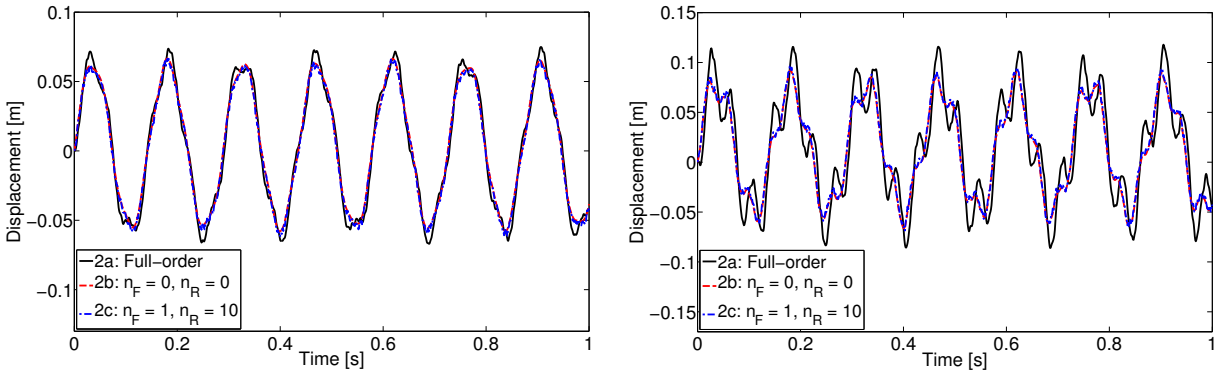

(a) Node 238 displacements (mid-chord, mid-span location on bottom surface).

(b) Node 247 displacements (mid-chord, tip location on bottom surface).

Figure 33. Comparison of z displacements at two locations under base excitation for full-order and ROM simulations.

IX. Concluding Remarks

A comprehensive study of structural dynamic response simulation within an aerothermoelastic analysis framework has been conducted with the goals of improving the computational efficiency and accuracy of the structural dynamic ROM. The study addressed three main modeling areas associated with structural dynamic reduced-order modeling in an aerothermoelastic framework:

- The effect of the transient temperature distribution due to aeroheating on the free vibration mode shapes and frequencies was examined
- A surrogate modeling technique was implemented to allow for direct updates to the temperature-dependent generalized stiffness matrix and thermal loads
- Load-dependent Ritz vectors were used to improve the accuracy of the structural dynamic ROM

In the first part of the study, the modal assurance criterion (MAC) was used to quantify the degree to which the natural mode shapes and frequencies of a representative hypersonic vehicle control surface change as a result of aerodynamic heating along a trajectory. This is motivated by the fact that the structural dynamic ROM uses a fixed set of basis vectors throughout the simulation, and the underlying assumption is therefore that the free vibration modes do not change significantly as a result of aeroheating. For the six modes tracked in this study, the MAC values of the first, second, fifth and sixth modes were found to remain close to one, indicating little change in those modes over time. However, a mode-switching phenomenon was found to occur between the third and the fourth modes. Though the third and fourth modes do evolve significantly over time, the overall modal content of modes three and four at room temperature is approximately the same as that at elevated temperature. Investigation into the evolution of natural frequencies over time shows a maximum departure from the room temperature natural frequency of 12% which occurs for mode 6. In cases where natural frequency has a significant impact on the overall system, the effect of aeroheating on natural frequencies must be considered.

The second part of this study focused on the development of a kriging-based method for directly updating the generalized stiffness matrix and thermal loads based on a given temperature distribution. The temperature distribution was parameterized in terms of the thermal POD modal coordinates as this allowed for a small number of design variables to be used to represent the high-dimensional temperature vector. A

methodology was described for bounding the POD modal coordinates based on a set of parallel aerothermoelastic simulations. A series of studies was used to guide the selection of various parameters involved in the generation of the kriging ROMs. The resulting ROMs of the generalized stiffness matrix and physical thermal load vector were found to have maximum L_∞ errors of 1% and 5%, respectively, over 500 evaluation points, indicating good agreement with the full-order model. Comparison of computation times showed that the structural ROM with the kriging models improved the computational cost of the structural dynamic response solution by a factor of five with respect to the full-order model.

To improve the accuracy of the structural ROM, basis augmentation using load-dependent Ritz vectors was examined. Load-dependent Ritz vectors are advantageous in that they allow for incorporation of the expected spatial dependence of the structural loads into the modal matrix. In order to determine the representative load vectors to be used in generating the load-dependent Ritz vectors, proper orthogonal decomposition was employed based on snapshots of the structural load vector from representative simulations. Application of the methodology for a hypersonic cruise trajectory demonstrated an average improvement in L_∞ error of 38% for one case compared with a case using only free vibration modes. In order to evaluate the performance of the methodology for cases with a larger degree of unsteadiness in the structural response, base motion was imposed at the control surface attachment point. Plots of the z displacements at two locations for one particular case illustrated that the ROM has difficulty capturing the response at the tip. Additionally, there was not a significant improvement in the ROM accuracy by including load-dependent Ritz vectors in this case. Future work will therefore focus on methods for improving the ROM error under base excitation loads.

Acknowledgment

This work was supported by the Michigan-AFRL Collaborative Center in Control Science (MACCCS) under grant number FA 8650-07-2-3744 (Air Force Research Laboratory/Air Vehicles Directorate) with Michael Bolender as program manager.

References

[1]Anderson, Jr., J. D., *Hypersonic and High-Temperature Gas Dynamics*, McGraw-Hill, 1989.

[2]Mei, C., Motagaly, K. A., and Chen, R., "Review of Nonlinear Panel Flutter at Supersonic and Hypersonic Speeds," *Applied Mechanics Review*, Vol. 52, No. 10, October 1999, pp. 321–332.

[3]Pourtakdoust, S. H. and Fazelzadeh, S. A., "Nonlinear Aerothermoelastic Behavior of Skin Panel with Wall Shear Stress Effect," *Journal of Thermal Stresses*, Vol. 28, No. 2, 2005, pp. 147–169.

[4]Gee, D. J. and Sipcic, S. R., "Coupled Thermal Model for Nonlinear Panel Flutter," *AIAA Journal*, Vol. 37, No. 5, May 1999, pp. 642–650.

[5]Dechaumphai, P., Thornton, E. A., and Wieting, A. R., "Flow-Thermal-Structural Study of Aerodynamically Heated Leading Edges," *Journal of Spacecraft and Rockets*, Vol. 26, No. 4, July–August 1989, pp. 201–209.

[6]Thornton, E. A. and Dechaumphai, P., "Coupled Flow, Thermal, and Structural Analysis of Aerodynamically Heated Panels," *Journal of Aircraft*, Vol. 25, No. 11, November 1988, pp. 1052–1059.

[7]Kontinos, D., "Coupled Thermal Analysis Method with Application to Metallic Thermal Protection Panels," *Journal of Thermophysics and Heat Transfer*, Vol. 2, No. 11, April–June 1997, pp. 173–181.

[8]McNamara, J. J., Friedmann, P. P., Powell, K. G., and Thuruthimattam, B. J., "Aeroelastic and Aerothermoelastic Behavior in Hypersonic Flow," *AIAA Journal*, Vol. 46, No. 10, October 2008, pp. 2591–2610.

[9]Culler, A. J. and McNamara, J. J., "Studies on Fluid-Thermal-Structural Coupling for Aerothermoelasticity in Hypersonic Flow," *AIAA Journal*, Vol. 48, No. 8, August 2010, pp. 1721–1738.

[10]Culler, A. J. and McNamara, J. J., "Coupled Flow-Thermal-Structural Analysis for Response Prediction of Hypersonic Vehicle Skin Panels," *Proceedings of the 51st AIAA/ASME/ASCE/AHS/ASC Structures, Structural Dynamics, and Material Conference, Orlando, Florida*, AIAA 2010-2965.

[11]Falkiewicz, N. J. and Cesnik, C. E. S., "A Reduced-Order Modeling Framework for Integrated Thermo-Elastic Analysis of Hypersonic Vehicles," *Proceedings of the 50th AIAA/ASME/ASCE/AHS/ASC Structures, Structural Dynamics, and Materials Conference, Palm Springs, California*, AIAA 2009-2308.

[12]Falkiewicz, N. J., Cesnik, C. E. S., Bolender, M. A., and Doman, D. B., "Thermoelastic Formulation of a Hypersonic Vehicle Control Surface for Control-Oriented Simulation," *Proceedings of the 2009 AIAA Guidance, Navigation, and Control Conference, Chicago, Illinois*, AIAA 2009-6284.

[13]Falkiewicz, N. J. and Cesnik, C. E. S., "Proper Orthogonal Decomposition for Reduced-Order Thermal Solution in Hypersonic Aerothermoelastic Simulations," *AIAA Journal*, In Press.

[14]Falkiewicz, N. J., Cesnik, C. E. S., Crowell, A. R., and McNamara, J. J., "Reduced-Order Aerothermoelastic Framework for Hypersonic Vehicle Control Simulation," *AIAA Journal*, Accepted February 2011.

[15]Falkiewicz, N. J. and Cesnik, C. E. S., "Proper Orthogonal Decomposition for Reduced-Order Thermal Solution in

Hypersonic Aerothermoelastic Simulations," *Proceedings of the 51st AIAA/ASME/ASCE/AHS/ASC Structures, Structural Dynamics, and Material Conference, Orlando, Florida*, AIAA 2010-2798.

[16]Eckert, E. R. G., "Engineering Relations for Friction and Heat Transfer to Surfaces in High Velocity Flow," *Journal of the Aeronautical Sciences*, Vol. 22, No. 8, March 23, 1955, pp. 585–587.

[17]Falkiewicz, N. J., Cesnik, C. E. S., Crowell, A. R., and McNamara, J. J., "Reduced-Order Aerothermoelastic Framework for Hypersonic Vehicle Control Simulation," *Proceedings of the 2010 AIAA Atmospheric Flight Mechanics Conference, Toronto, Ontario, Canada*, AIAA 2010-7928.

[18]Holmes, P., Lumley, J., and Berkooz, G., *Turbulence, Coherent Structures, Dynamical Systems and Symmetry*, Cambridge University Press, 1996.

[19]Liang, Y. C., Lee, H. P., Lim, S. P., Lin, W. Z., Lee, K. H., and Wu, C. G., "Proper Orthogonal Decomposition and its Applications–Part I: Theory," *Journal of Sound and Vibration*, Vol. 252, No. 3, 2002, pp. 527–544.

[20]Sirovich, L., "Turbulence and Dynamics of Coherent Structures, Part I: Coherent Structures," *Quarterly of Applied Mathematics*, Vol. XLV, 1987, pp. 561–571.

[21]Craig, R. R. and Kurdila, A. J., *Fundamentals of Structural Dynamics*, John Wiley & Sons, Inc., 2nd ed., 2006.

[22]MSC.Software Corporation, Santa Ana, CA, *MSC.Nastran Basic Dynamic Analysis User's Guide: Version 68*, 2004.

[23]Crowell, A. R., McNamara, J. J., Kecskemety, K. M., and Goerig, T. W., "A Reduced Order Aerothermodynamic Modeling Framework for Hypersonic Aerothermoelasticity," *Proceedings of the 51st AIAA/ASME/ASCE/AHS/ASC Structures, Structural Dynamics, and Material Conference, Orlando, Florida*, AIAA 2010-2798.

[24]Oppenheimer, M. W. and Doman, D. B., "A Hypersonic Vehicle Model Developed with Piston Theory," *Proceedings of the 2006 AIAA Atmospheric Flight Mechanics Conference, Keystone, Colorado*, AIAA 2006-6637.

[25]Pendleton, E., Moster, G., and Keller, D., "Transonic Aeroelastic Models of Highly Swept Hypersonic Lifting Surfaces," *Journal of Aircraft*, Vol. 32, No. 6, Nov. - Dec. 1995, pp. 1169–1176.

[26]McNamara, J. J., *Aeroelastic and Aerothermoelastic Behavior of Two and Three Dimensional Lifting Surfaces in Hypersonic Flow*, Ph.D. thesis, University of Michigan, Ann Arbor, Michigan, 2005.

[27]Shih, P., Prunty, J., and Mueller, R., "Thermostructural Concepts for Hypervelocity Vehicles," *Journal of Aircraft*, Vol. 28, No. 5, May 1991, pp. 337–345.

[28]Myers, D., Martin, C., and Blosser, M., "Parametric Weight Comparison of Advanced Metallic, Ceramic Tile, and Ceramic Blanket Thermal Protection Systems," Tech. Rep. NASA TM-210289, Langley Research Center, June 2000.

[29]Wieting, A., Dechaumphai, P., Bey, K., Thornton, E., and Morgan, K., "Application of Integrated Fluid-Thermal-Structural Analysis Methods," *Thin-Walled Structures*, Vol. 11, No. 1-2, 1991, pp. 1–23.

[30]Blevins, R., Bofilios, D., Holehouse, I., Hwa, V., Tratt, M., Laganelli, A., Pozefsky, P., and Pierucii, M., "Thermo-Vibro-Acoustic Loads and Fatigue of Hypersonic Flight Vehicle Structure," Tech. Rep. AFRL-RB-WP-TR-2009-3139, Air Force Research Laboratory, June 2009.

[31]Ellis, D., Pagel, L., and Schaeffer, D., "Design and Fabrication of a Radiative Actively Cooled Honeycomb Sandwich Structural Panel for a Hypersonic Aircraft," Tech. Rep. NASA-CR-2957, NASA, March 1978.

[32]Leyens, C. and Peters, M., *Titanium and Titanium Alloys: Fundamentals and Applications*, Wiley-VHC, 2003.

[33]Department of Defense, *Military Handbook - MIL-HDBK-5H: Metallic Materials and Elements for Aerospace Vehicle Structures*, December 1998.

[34]Welsch, G., Boyer, R., and Collings, E. W., *Materials Properties Handbook: Titanium Alloys*, ASM International, 1994.

[35]Allemenag, R. J. and Brown, D. L., "A Correlation Coefficient for Modal Vector Analysis," *Proceedings of the International Modal Analysis Conference*, 1982, pp. 110–116.

[36]Sacks, J., Welch, W. J., Mitchell, T. J., and Wynn, H. P., "Design and Analysis of Computer Experiments," *Statistical Science*, Vol. 4, No. 4, 1989, pp. 409–435.

[37]Simpson, T. W., Mauery, T. M., Korte, J. J., and Mistree, F., "Kriging Models for Global Approximation in Simulation-Based Multidisciplinary Design Optimization," *AIAA Journal*, Vol. 39, No. 12, December 2001, pp. 2233–2241.

[38]Sasena, M. J., *Flexibility and Efficiency Enhancements for Constrained Global Design Optimization with Kriging Approximations*, Ph.D. thesis, University of Michigan, Ann Arbor, Michigan, 2002.

[39]Wilson, E. L., Yuan, M.-W., and Dickens, J. M., "Dynamic Analysis by Direct Superposition of Ritz Vectors," *Earthquake Engineering & Structural Dynamics*, Vol. 10, No. 6, Nov. – Dec. 1982, pp. 813–821.

[40]Frendreis, S. G. V. and Cesnik, C. E. S., "3D Simulation of Flexible Hypersonic Vehicles," *Proceedings of the 2010 AIAA Atmospheric Flight Mechanics Conference, Toronto, Ontario, Canada*, AIAA 2010-8229.